

**NASA
Technical
Paper
3383**

July 1993

9-14-93
K-7662

**Laser Anemometer Measurements
and Computations for Transonic
Flow Conditions in an Annular
Cascade of High Turning Core
Turbine Vanes**

Louis J. Goldman

NASA

**NASA
Technical
Paper
3383**

1993

Laser Anemometer Measurements
and Computations for Transonic
Flow Conditions in an Annular
Cascade of High Turning Core
Turbine Vanes

Louis J. Goldman
*Lewis Research Center
Cleveland, Ohio*



National Aeronautics and
Space Administration

Office of Management

Scientific and Technical
Information Program

Trade names or manufacturers' names are used in this report for identification only. This usage does not constitute an official endorsement, either expressed or implied, by the National Aeronautics and Space Administration.

Summary

An advanced laser anemometer (LA) was used to measure the mean axial and tangential velocity components in an annular cascade of turbine stator vanes operating at transonic flow conditions. The vanes tested were based on a previous redesign of the first-stage stator in a two-stage turbine for a high-bypass-ratio engine. The vanes produced 75° of flow turning. Tests were conducted on a 0.771-scale model of the engine-sized stator. The advanced LA fringe system employed an extremely small 50- μm -diameter probe volume. This smaller size allowed the laser power to be more concentrated in the probe volume, permitting measurements to be obtained from smaller seed particles and closer to surfaces. Beam correction optics were employed to prevent the beams from uncrossing in passing through the curved optical access window. In addition, the access window was manufactured to the same high quality as the other optical components used in the LA system.

A particle dynamics calculation was performed for this vane geometry and operating condition to determine how well seed particles tracked the airflow. Seed particles of 0.5- μm diameter, which represented the bulk of the aerosol generated by the seeder, followed the flow to within ± 0.75 percent (of the critical velocity ratio) in both the axial and tangential velocity components. Seed particles of 1- μm diameter, which were near the upper end of the seed particle distribution, generally followed the flow to within ± 1.5 percent (of the critical velocity ratio) in both velocity components. However, differences of -2.5 percent in the tangential velocity component were indicated close to the suction surface of the vanes near the leading-edge region.

Experimental LA measurements of velocity and turbulence were obtained at the mean radius upstream of, within, and downstream of the stator vane row at an exit critical velocity ratio of 1.050 at the hub. In addition, a radial survey was taken at the upstream location to determine the boundary layer thickness. Surface static pressure measurements were also obtained near the vane hub, at midspan, and near the tip. The measurements were compared, where possible, with the results from Denton's three-dimensional inviscid flow analysis program. Comparisons were also made with the results

obtained previously when these same vanes were tested at the design exit critical velocity ratio of 0.896 at the hub. The data are presented in both graphical and tabulated form so that they can be readily compared against other turbomachinery computations.

The experimental measurements of vane surface static pressures compared well with the calculated values. Comparing the transonic and design flow results indicated little difference on the vane pressure surface until about 90-percent axial chord. However, on the vane suction surface the measurements deviated from each other from about 50-percent axial chord until the trailing edge. The maximum free-stream critical velocity ratio of 1.12 occurred near the hub on the vane suction surface at about 80-percent axial chord.

At the upstream location (-100 -percent axial chord) the LA measurements indicated that the flow at the mean radius was circumferentially uniform and axial in direction, in accordance with the mixed-out calculated value. Comparing the transonic and design flow measurements showed only very slight differences in the axial components. At this location the measured boundary layer thickness was 8.1 and 9.3 percent of vane height at the tip and hub endwalls, respectively. Laser anemometer measurements could be made to about 2 percent of the tip endwall and 3 percent of the hub endwall. At -25 - and -10 -percent axial chord the effect of the vane leading edge was seen, and the agreement between the measurements and the theory was very good to excellent.

From the vane leading edge to 60-percent axial chord the agreement between the measurements and the theory was very good to excellent. From 70-percent axial chord to the vane trailing edge the tangential velocity component measurements were somewhat lower than the calculations, particularly near the vane suction surface. Comparing the transonic and design flow results showed significant differences in the tangential components after the 50-percent axial chord position.

The measurements downstream of the vanes but close to the trailing-edge plane clearly indicated the location of the vane wake. The wake deficit dissipated rapidly in moving downstream of the trailing edge and was hard to delineate at 75-percent axial chord downstream of the vanes. Outside of

the wake regions the measurements agreed reasonably with the inviscid calculations, although the tangential component values were still lower than the calculations. Comparing the transonic and design flow results showed, as expected, differences in both the tangential and axial components downstream of the vanes.

In general, the turbulence intensity of the flow varied 3 to 4 percent upstream of the vanes, 2 to 3 percent within the vane passage, and 4 to 6 percent downstream of the vanes. Within the vane wakes turbulence levels as high as 9 to 10 percent were measured.

Introduction

State-of-the-art turbofan engines are characterized by high bypass ratios, resulting in high-pressure turbines designed for high specific work and low equivalent flows. These characteristics can easily produce turbines that have high hub-to-tip radius ratios, low aspect ratios, and transonic flows. All of these conditions can be detrimental to engine performance. To reduce these problems, designers are often forced to specify high turning vanes with increased blade heights and lower throughflow velocities. Typical turbines of this type are described in references 1 to 3 as part of the NASA Energy Efficient Engine Program. High turning vanes are also finding use in modern turboshaft applications, as well as in space applications (ref. 4).

However, the use of high turning vanes can result in other problems, such as large secondary flows or possibly flow separation. These problems become even more severe if the flow is transonic. Computer code validation of these adverse conditions is difficult because experimental measurements of the internal flow characteristics in these situations are not commonplace. Some experimental data have been obtained for high turning transonic vanes by using pressure probes (refs. 5 and 6) and for high turning subsonic vanes by using laser anemometry (refs. 7 and 8). But experimental results obtained within the passages of high turning transonic vanes are scarce, especially with details of the vane geometry included.

In order to add to the experimental data base available for comparison with computational fluid dynamics analyses, an investigation was performed in an annular cascade of turbine stator vanes designed to produce 75° of flow turning. The initial subsonic tests were accomplished with the cascade operating at the vane design exit critical velocity ratio of 0.896 at the hub. For these conditions laser anemometer measurements were reported previously in reference 8. For the transonic investigation reported herein the facility was operated at an exit critical velocity ratio of 1.050 at the hub. This corresponded to the maximum velocity level possible for these vanes without extensive modification of the facility hardware.

An advanced laser anemometer (LA) that was used in the previous subsonic tests (ref. 8) was also used for this investigation. The LA consisted of a fringe system that employed an extremely small 50- μm -diameter probe volume. This smaller size allowed the laser power to be more concentrated in the probe volume, permitting measurements to be obtained from smaller seed particles and closer to surfaces.

This report presents the results of laser anemometer measurements of velocity and turbulence taken upstream of, within, and downstream of a 75° flow-turning vane operating at transonic flow conditions. The data obtained represent the results of 23 circumferential surveys taken at constant axial positions in the annular cascade at the mean radius. In addition, a radial survey was taken at the upstream location to determine the boundary layer thickness. Surface static pressure measurements were also obtained near the vane hub and tip and at midspan. The measurements were compared, where possible, with the calculations obtained from Denton's three-dimensional inviscid flow analysis program (ref. 9). This flow analysis was previously compared with the laser anemometer measurements obtained for these vanes tested at design (subsonic) conditions (ref. 8). Comparisons are also presented between the results obtained at transonic and design conditions. The data are presented herein in both graphical and tabulated form, allowing the measurements to be easily compared with other turbomachinery computations.

Symbols

LE	leading edge of vane
m	number of transverse velocity component measurements (typically 1000)
P	total pressure, N/m^2
p	static pressure, N/m^2
R	radial position, percent of span from hub
s_j^2	variance of velocity component measurements (eq. 5), $(\text{m/s})^2$
TE	trailing edge of vane
Tu	turbulence intensity (eq. (4))
V	transverse velocity magnitude (fig. 7), m/s
V_{cr}	critical velocity (fluid velocity at Mach 1), m/s
V_j	measured velocity component (fig. 7), m/s

V_z	axial velocity component, m/s
V_θ	tangential velocity component, m/s
v'	velocity fluctuations, m/s
y	distance from endwall, m
Z	axial position, percent of axial chord from vane leading edge
α	flow angle measured from axial direction (eq. (3); fig. 7), deg
δ	boundary layer thickness, m
θ	circumferential position, deg
σ	standard deviation of velocity component measurements, m/s
ϕ_j	fringe orientation angle, angle between z axis and measured velocity component (fig. 7), deg

Subscripts:

fs	free stream
g	gas (air)
h	hub
M	mixed-out station (fig. 2)
p	seed particle
PS	pressure surface
SS	suction surface
0	station at inlet plane of cascade bellmouth (fig. 2)

Superscript:

$-$	mean value
-----	------------

Apparatus

Annular Cascade Facility

The 508-mm-tip-diameter, full-annular, turbine stator cascade includes an inlet section, a test section, and an exit section. A photograph and a cross-sectional view of the facility

are shown in figures 1 and 2, respectively. In operation, atmospheric air is drawn through the inlet section, the vanes, and a dump-diffusing exit section and then exhausted through the laboratory altitude exhaust system. Before entering the altitude exhaust system the flow passes through a flow-straightening section that removes the swirl created by the stator vanes.

Inlet section.—The inlet, consisting of a bellmouth and a straight section, was designed to accelerate the flow to uniform axial-flow conditions at the vane inlet. The bellmouth profile and coordinates are presented in reference 10.

Test section.—The test section, for this and the previous investigation, consisted of a full-annular ring of 26 vanes. A cutout in the outer cascade housing provided access for the laser beams to the vane passage, as well as the regions upstream and downstream of the vanes. The vanes in these regions were machined to the vane tip radius so that the window would fit flush with the tip endwall. The window is described in the next section.

The stator vane geometry and coordinates are shown in figure 3 and are the same vanes that were tested at design conditions (ref. 8). These vanes were a second-generation design. The original vanes were designed (ref. 1) to be the first-stage stator in a two-stage, high-bypass-ratio turbine. Geometrically, the new vanes had a thinner trailing-edge radius (0.051 cm compared with 0.089 cm) and a slightly

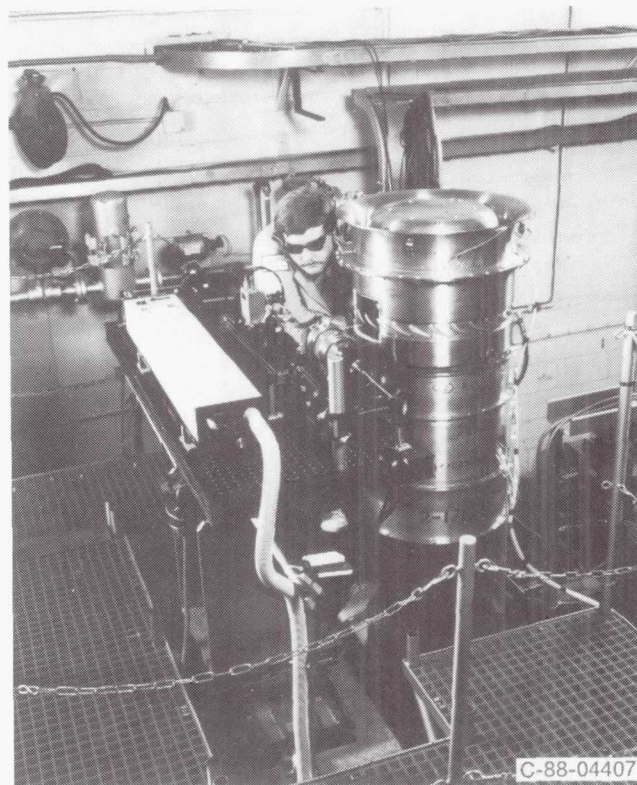


Figure 1.—Core turbine stator annular cascade and laser anemometer.

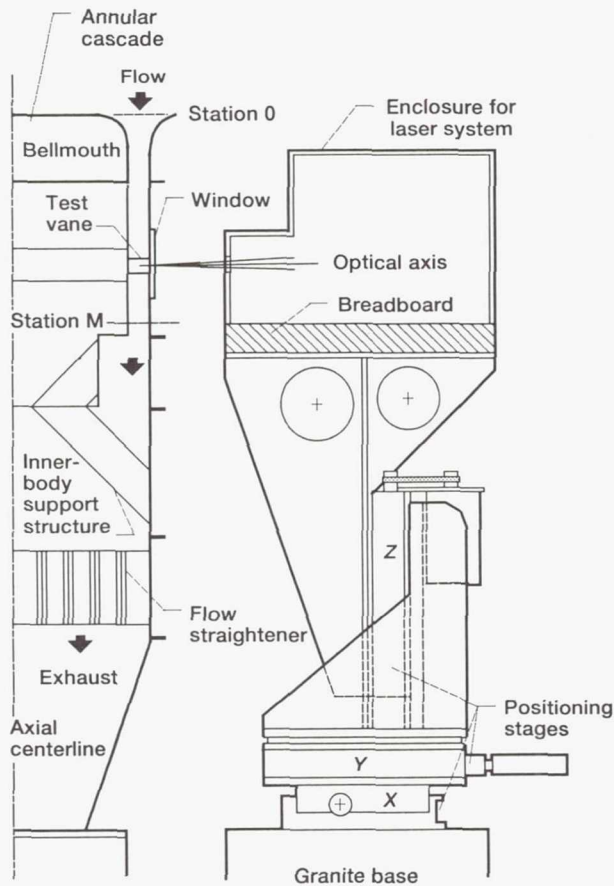
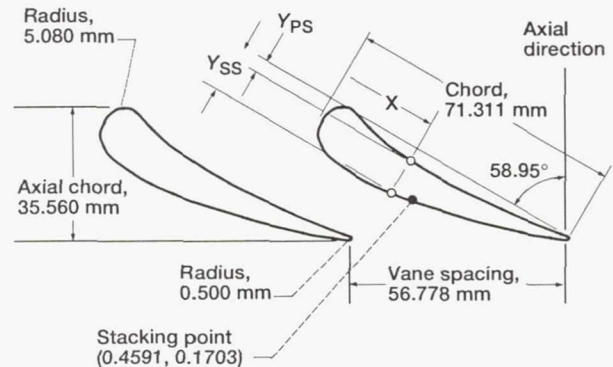


Figure 2.—Schematic cross-sectional view of core turbine stator cascade and laser positioning system.

different pressure surface shape to accommodate the new trailing edge. The untwisted vanes, of constant profile from hub to tip, were stacked at a point on the suction surface, as indicated in figure 3. The vanes had an axial chord of 35.56 mm and a vane height of 38.10 mm. This resulted in a vane aspect ratio and solidity at the mean radius (based on axial chord) of 1.07 and 0.63, respectively. The vane height was slightly larger than that used in reference 1 (35.64 mm) and was chosen to minimize changes in the existing cascade hardware. The cascade was designed for a stator with a hub-to-tip radius ratio of 0.85 and a tip radius of 508 mm. The vanes in this investigation represented a 0.771-scale model of the engine-sized stator (as compared with 0.767 in ref. 1).

Window.—Optical access for the laser beams was provided by a cutout in the cascade housing (fig. 1) that extended upstream and downstream of the vane passage by approximately two and one axial chord, respectively. The window was optically manufactured, under standard lens tolerances, from 3.175-mm-thick optical glass. This was thought necessary because of the smaller laser probe volume employed in the optical design and the possibility that the beams would uncross on passing through the window. A silicone rubber sealing material was used both to seal the window to the cascade housing and to seal the vane tips to the



All values nondimensionalized by chord, 71.311 mm (2.8075 in.).

X	Y _{PS}	Y _{SS}	X	Y _{PS}	Y _{SS}
0	0.0712	0.0712	0.5343	0.0493	0.1532
.0178	.0241	.1231	.5521	.0485	.1488
.0358	.0095	.1460	.5699	.0475	.1443
.0534	.0023	.1616	.5877	.0464	.1397
.0712	0	.1728	.6055	.0453	.1350
.0890	.0023	.1810	.6233	.0440	.1301
.1069	.0085	.1871	.6411	.0426	.1252
.1247	.0145	.1918	.6589	.0411	.1202
.1425	.0198	.1953	.6768	.0396	.1151
.1603	.0245	.1979	.6946	.0379	.1099
.1781	.0286	.1996	.7124	.0362	.1047
.1959	.0323	.2007	.7302	.0344	.0993
.2137	.0356	.2011	.7480	.0325	.0939
.2315	.0384	.2010	.7658	.0305	.0884
.2493	.0410	.2004	.7836	.0285	.0829
.2671	.0431	.1994	.8014	.0264	.0773
.2850	.0450	.1980	.8192	.0242	.0717
.3028	.0466	.1962	.8370	.0220	.0660
.3206	.0480	.1942	.8549	.0197	.0603
.3384	.0491	.1919	.8727	.0173	.0545
.3562	.0500	.1893	.8905	.0149	.0487
.3740	.0507	.1865	.9083	.0124	.0428
.3918	.0512	.1835	.9261	.0099	.0369
.4096	.0515	.1802	.9439	.0073	.0310
.4274	.0516	.1768	.9617	.0047	.0250
.4452	.0516	.1732	.9795	.0020	.0189
.4630	.0514	.1695	.9973	.0015	.0125
.4809	.0511	.1656	1.0000	.0070	.0070
.4987	.0507	.1616			
.5165	.0500	.1574			

Figure 3.—High turning core turbine stator vane geometry at mean section.

window. The window covered about 36° in the circumferential direction and had an axial length of 140 mm.

Laser Anemometer System

An advanced laser anemometer that had been used in the previous subsonic tests (ref. 8) was also used for this investigation. The LA consisted of a fringe system that employed an extremely small 50- μm -diameter probe volume. The optics, positioning system, and seeding technique used in the investigation are briefly described in this section. Further details can be found in reference 8.

Optical layout.—A photograph of the laser anemometer and a schematic of the optical layout are shown in figures 1 and 4, respectively. The argon-ion laser has a maximum output power of 1.5 W at a 514.5-nm wavelength. Lenses L1 and L2 function as mode-matching lenses to position the beam waists at the focal plane of lens L5. The beam divider splits the single beam into two equal-intensity parallel beams with approximately 10-mm separation. The divider is mounted in a motor-driven rotary mount, so that the fringes can be oriented at any desired angle. A gear-driven, half-wave retardation plate is located at the input of the beam divider to maintain the proper linear polarization there. After reflection from mirrors M3 and M4 the parallel beams from the beam splitter are expanded by lenses L3 and L4 to approximately 25-mm spacing. Mirror M4 is elliptical to minimize its blocking of the scattered light collected by the receiving optics. The beams are then focused by lens L5 (250-mm focal length) to cross at the probe volume after being reflected by mirror M7. Mirror

M7 is mounted on a motor-driven goniometer stage with axis perpendicular to the plane of the optical table. This enables the optical axis to be maintained along the radial direction in the cascade during circumferential surveys. The diameter ($1/e^2$ intensity) of the probe volume is about 50 μm , and the fringe spacing is 5.2 μm (about 10 fringes). The technique used to measure the fringe spacing is described in appendix B of reference 11. Light that is scattered from seed particles passing through the probe volume (after reflection by mirror M7) is collimated by lens L5 and reduced to a 40-mm-diameter parallel beam by lenses L4 and L3. A central circular stop (CS) placed between mirror M4 and lens L6 is used to reduce the effective length of the probe volume. This mask blocks 64 percent of the full clear aperture of the collection lens L5, which means that the receiving optics has an effective f-number for light collection of $f/4.2$. The scattered light beam is focused by lens L6 through a 100- μm -diameter pinhole (PH) located in front of the photomultiplier tube (RCA 4526). The system magnification of 2 results in the image of the pinhole at the probe volume having a 50- μm diameter. The signal from the photomultiplier tube is processed by a TSI, Inc., counter type of signal processor to provide velocity components transverse to the optical axis.

Cylindrical lens C1 is used to correct the astigmatism introduced by the window (ref. 12). This ensures that the two beams cross at the probe volume for all orientations of the fringe pattern. The cylindrical lens C1 was custom designed for this application. It is mounted on a remotely controlled linear translation stage with the cylinder axis perpendicular to the optical table. (The axial position of the lens needed to minimize the astigmatism is a function of the distance of the probe volume from the window.)

Positioning system.—The laser and optics are mounted on a 610-mm by 1524-mm by 64-mm-thick aluminum optical breadboard. The breadboard is mounted on a three-axis linear positioning system with an accuracy of $\pm 2.5 \mu\text{m}$ per 25 mm of travel (not to exceed $\pm 12 \mu\text{m}$ per 300 mm). The ANORAD Corporation positioning system controller is located in the test cell near the cascade and is connected with an RS-232 serial communications link to a computer located in the control room. In addition to the three linear stages the beam divider and the goniometer-mounted mirror are also controlled with this system. This control provides a sufficient number of degrees of freedom to allow the optical axis to be directed along a radial line throughout the test region. The cylindrical lens in the window correction optics is positioned with a separate Newport Corporation linear actuator and translation stage.

Seeding.—An organic aerosol (Rosco fog/smoke fluid) was used as the seed material for these tests. The fluid was atomized with a commercial TSI, Inc., six-jet aerosol generator. The seed was then passed through a separator to remove any large droplets before being injected through a 6-mm-diameter tube into the flow at the bellmouth entrance. The seed particle size distribution over a range of 0.09- to 3.00- μm diameter was previously measured (ref. 8) at the bellmouth entrance by

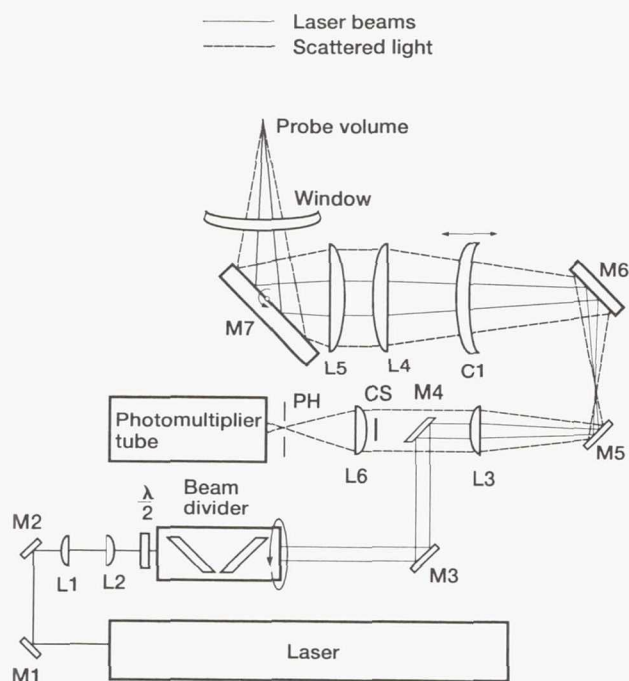


Figure 4.—Optical layout of laser anemometer measurement system.

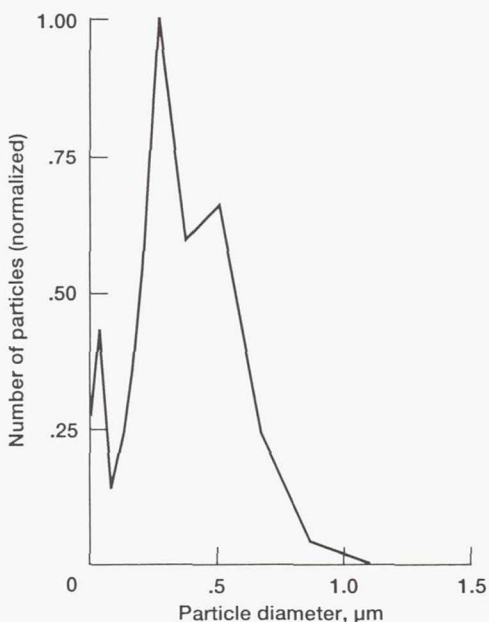


Figure 5.—Measured seed particle size distribution.

using a Particle Measuring Systems, Inc., laser aerosol spectrometer. The results shown in figure 5 indicate that most of the seed particles produced are between 0.3- and 0.6- μm diameter with few greater than 1.0 μm .

Calibration procedures.— A critical requirement for obtaining laser anemometer data for computer code verification is the accurate determination of the probe volume location relative to the experimental hardware. For the stator cascade described in this report, location accuracies of 25 μm are desired. A complicating factor in achieving this accuracy is that the stator cascade moves relative to the laser anemometer when going from static to flow conditions and when the ambient temperature changes. For these reasons the position calibration must be checked under test conditions. The parameters required are the coordinates of the cascade axes, the radial position of the hub endwall, and the circumferential location of the vane suction and pressure surfaces at a given axial and radial position. Most calibration procedures used in this investigation are described in detail in appendix B of reference 11. One additional calibration technique was required to determine the position of the window correction optics relative to the cascade; it is described in reference 8. The calibration procedures will not be discussed further herein.

Test Procedure

Cascade Flow Conditions

The test conditions in the cascade were set by controlling the pressure ratio across the vane row with two throttle valves located in the exhaust system. A hub static tap located

downstream of the test section, where the flow was assumed to be nearly circumferentially uniform (station M, fig. 2), was used to set this pressure ratio. For this investigation the exit hub-static to inlet-total pressure ratio $p_{h,M}/P_0$ was maintained at 0.491. This corresponds to a critical velocity ratio of 1.050.

Because of the transonic flow conditions and the necessity of using room air, condensation was observed in the cascade on warm and/or humid days. Generally, the condensation occurred downstream of the vane trailing edge and extended outward from the hub endwall up through the mean radius. Condensation did not appear to occur near the tip endwall or within the vane passage. The light that was scattered from the condensation particles could easily be seen by eye by placing the laser probe volume in this condensation area. However, the signal-to-noise ratios were too small to allow processing by the TSI counter processor. Laser anemometer measurements were not attempted if condensation occurred anywhere near the mean radius. Measurements were made only on cool and dry days, when the slight condensation occurring near the hub endwall was not considered significant.

Survey Measurement Locations

The locations of the laser anemometer survey measurements are summarized in figure 6. Circumferential surveys were made at 11 axial stations (every 10 percent of axial chord) within the vane passage, 4 axial stations upstream, and 5 axial stations downstream of the vanes. The nomenclature and orientation of the velocity component measurements are shown in figure 7. At a given axial station laser surveys were made across the vane passage, at the mean radius, with circumferential increments of 0.5° . Because multiple data sets were obtained at axial locations near the trailing edge, a total of 23 circumferential surveys are reported containing about 550 distinct measurement points. At every fixed point in the flow field seven components of the transverse velocity V_j were measured at 10° intervals centered about the expected flow direction (fig. 7). These measurements were made by rotating the beam divider and thereby changing the fringe orientation angle ϕ_j . This not only allowed the axial and tangential velocity components to be determined by a least-squares procedure, but it also provided an estimate of their statistical accuracy.

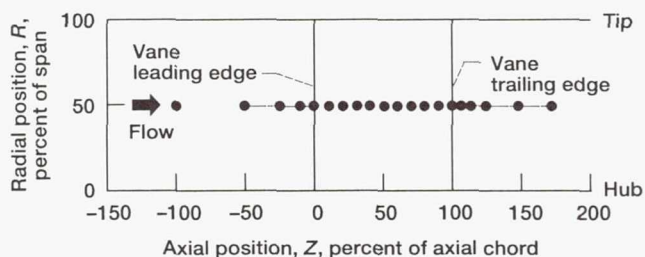


Figure 6.—Laser survey measurement locations.

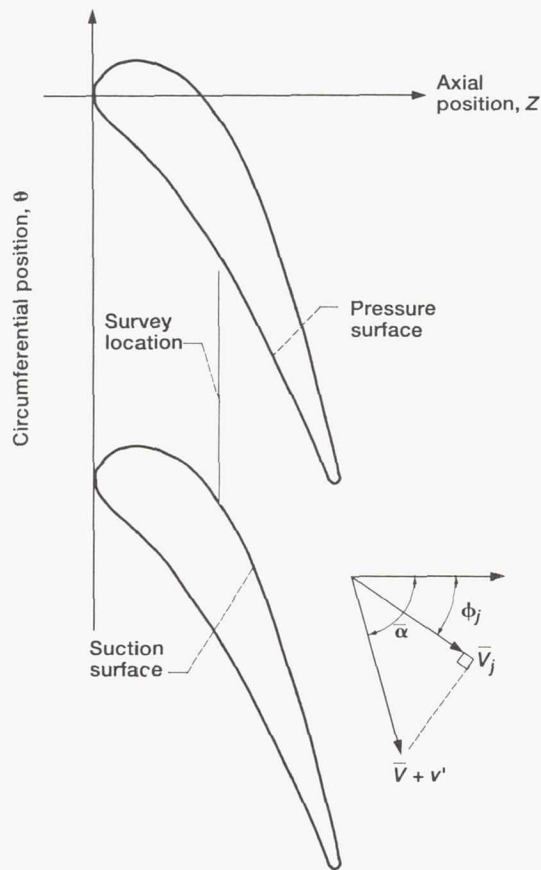


Figure 7.—Nomenclature of velocity component measurements for laser anemometer surveys.

In addition, a radial survey was made at the upstream location (–100-percent axial chord) to determine the boundary layer characteristics of the entering flow.

Data Acquisition

An IBM PS/2 Model 80 computer was used to control the optical positioning system and to acquire the laser anemometer data. The fringe signal from the photomultiplier tube was processed with a TSI counter processor by using four cycles of the Doppler burst. The counter output data, consisting of Doppler frequency and time between measurements, were transferred to the computer through a direct memory access (DMA) interface. As stated previously, data were taken at seven fringe orientations for each measurement position. At each fringe orientation 1000 data pairs were taken. The frequency data (corresponding to velocity components) were stored in 256-bin histograms for later off-line processing. Typical data rates ranged from 5 to 50 kHz.

Calculation Procedures

Experimental

The measured fringe spacing ($5.2 \mu\text{m}$) was used to calculate the mean velocity component \bar{V}_j and the variance s_j^2 from the stored 256-bin frequency histogram. This was done for the seven fringe orientation angles ϕ_j at each measurement location. The mean axial velocity component \bar{V}_z and the mean tangential velocity component \bar{V}_θ (of the projection of the velocity vector in the axial-tangential plane, fig. 7) were then obtained by using a procedure similar to that described in references 8 and 13. That is, \bar{V}_z and \bar{V}_θ were found by using a least-squares fit of the data to the equation

$$\bar{V}_j = \bar{V}_z \cos \phi_j + \bar{V}_\theta \sin \phi_j \quad (1)$$

In addition, the least-squares fit provided an estimate of the statistical uncertainty in the calculated velocity components.

The mean transverse velocity magnitude \bar{V} and mean flow angle can be calculated from

$$\bar{V} = \sqrt{\bar{V}_z^2 + \bar{V}_\theta^2} \quad (2)$$

$$\bar{\alpha} = \arctan\left(\frac{\bar{V}_\theta}{\bar{V}_z}\right) \quad (3)$$

The turbulence intensity Tu of the flow was calculated by assuming isotropic turbulence, as well as negligible noise from the laser, from

$$\text{Tu} = \frac{\sqrt{\overline{(v')^2}}}{\bar{V}} \quad (4)$$

The mean velocity fluctuations $\overline{(v')^2}$ for isotropic turbulence were obtained by a least-squares fit of (see ref. 13)

$$S_j^2 = \frac{1}{m} \sum_{j=1}^m (V_j - \bar{V}_j)^2 = \overline{(v')^2} [1 - \sin 2(\bar{\alpha} - \phi_j)] \quad (5)$$

It was assumed that $\bar{\alpha}$ had been determined previously by using equation (3).

At the upstream location (one axial chord from the vane leading edge) the radial survey measurements were further least-squares fit to a 1/7th power law profile given by

$$\frac{\bar{V}_z}{V_{fs}} = \left(\frac{y}{\delta}\right)^{1/7} \quad (6)$$

The boundary layer thickness δ was determined separately for the hub and tip endwalls.

Theoretical

Theoretical calculations were performed to determine the velocity of the air flowing through the vane passage and to determine how well the entrained seed particles used for the laser anemometer measurements tracked the airflow.

Air velocity.—The velocity field for the 75° turning vane was calculated by using Denton's three-dimensional inviscid flow analysis program (ref. 9). Denton's program is a time-marching, finite-volume solution of the Euler equations. The static pressure is specified at the downstream hub location, and the spanwise pressure variation is calculated by the program, assuming zero meridional streamline curvature (simple radial equilibrium). Cusps are placed at the leading and trailing edges of the vanes to minimize discontinuities in the grid slope. The cusps carry no load and therefore flow periodicity is automatically satisfied by the program. Denton's calculations were selected for comparison with the experimental data reported herein because they were found to compare well with the laser measurements obtained previously (refs. 8, 11, and 13) in this cascade.

Seed particle velocity.—A dynamics calculation was performed for this vane geometry and operating condition to determine how well different-sized seed particles tracked the airflow. The seed particle trajectories were calculated for a mean-radius, blade-to-blade stream surface by the method described in reference 14. It was assumed for these calculations that the seed particles are moving through a known airflow (velocity field), that the particles are acted upon only by viscous drag forces, and that these forces follow Stoke's law. The particle concentration is also low enough so as not to influence the airflow or the air properties. In addition, the seed particles are spherical, of uniform size, noninteracting, and uniformly distributed in the airflow. The difference between the calculated particle velocity and the airflow velocity, at a given point, is an estimate of how well the particles (of assumed size) follow the flow.

Results and Discussion

Seed Particle Velocity

The results of the seed particle dynamics calculation are shown in figure 8 for 0.5- and 1- μm -diameter particles. Results are presented for both the axial and tangential components of velocity because this is the form used for the experimental LA measurement presentations. Contour lines in this figure are shown as differences in the seed particle and the airflow component velocities normalized by the critical veloc-

ity. Negative contour levels therefore represent seed particles lagging the airflow.

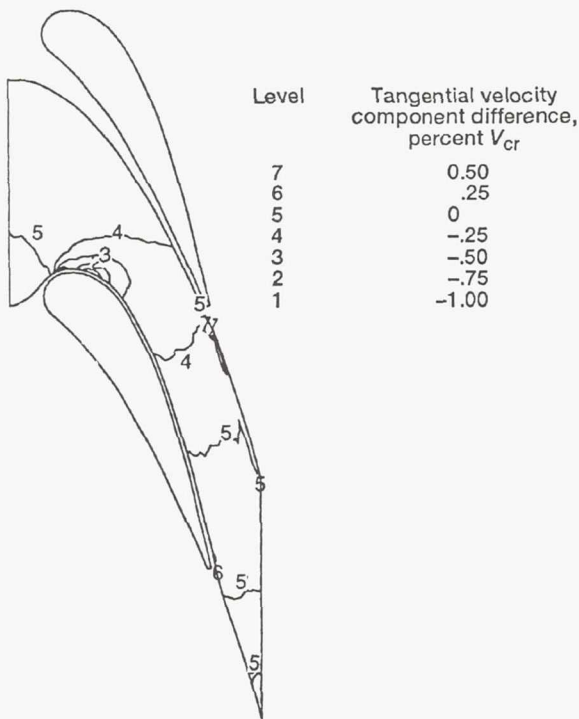
The 0.5- μm -diameter particles represent the size of the bulk of the aerosol generated (see fig. 5). These results (figs. 8(a) and (b)) indicated that differences in the seed particle and airflow velocities are less than ± 0.75 percent (in critical velocity ratio) in both components, with most of the flow less than ± 0.25 percent. The 1- μm -diameter particles are near the upper end of the seed particle distribution produced by the aerosol generator (fig. 5). The results of these dynamic calculations represent an estimate of the maximum lag problems that can occur in the LA measurements. In general, the contour levels for both velocity components are less than ± 1.5 percent (figs. 8(c) and (d)). However, tangential velocity component contours of -2.5 percent exist close to the vane suction surface near the leading-edge region. These differences are somewhat higher than were previously calculated at the design flow conditions (ref. 8). This result was expected because larger accelerations occurred in this region for the transonic flow conditions.

Surface Static Pressure Measurements

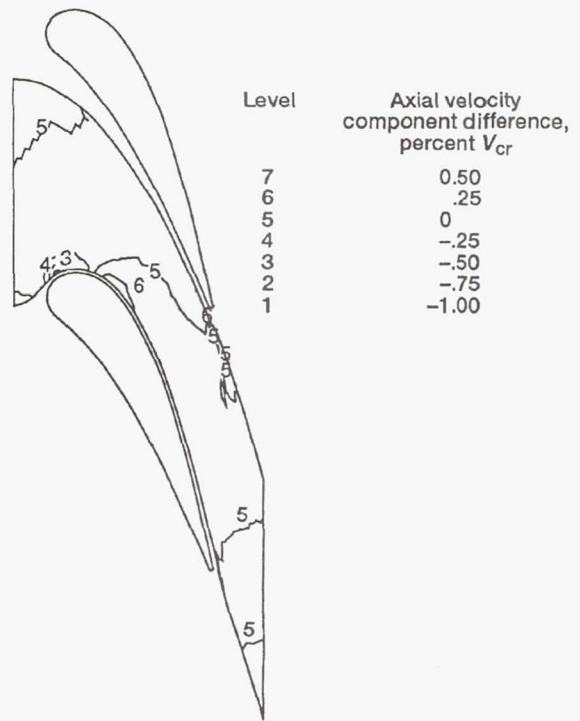
Static pressures were measured on the vane surface for radial positions of 6.7, 50, and 93.3 percent of span and are presented in figure 9 as free-stream critical velocity ratios. The experimental pressure ratio measurements are also given in table I. Comparing the vane surface measurements with the theoretical results from Denton's inviscid flow analysis program generally shows good agreement. Comparing the transonic and design flow results indicates very little difference on the vane pressure surface until about 90-percent axial chord. However, on the vane suction surface the distributions deviate from each other from about 50-percent axial chord to the trailing edge. A maximum free-stream critical velocity ratio of 1.12 was measured near the hub on the vane suction surface at about 80-percent axial chord.

Laser Survey Measurements

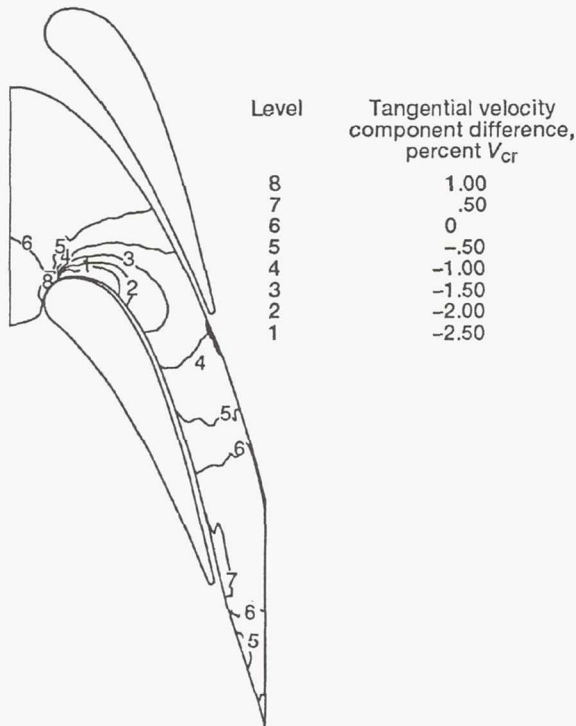
Results of the laser survey measurements are shown in figures 10 to 15 and are presented in tables II and III. For the radial survey upstream of the vanes (fig. 10) the experimental data are presented as axial-to-free-stream velocity ratio as a function of distance from the endwall normalized by the boundary layer thickness. For the laser circumferential survey measurements (figs. 11 to 15) the experimental data are presented as axial and tangential critical velocity ratios as a function of circumferential position. The estimated statistical uncertainties of the measurements (as determined from the least-squares fit by the methods described in ref. 13) are plotted in these figures as 2σ confidence intervals. If a confidence interval is not shown for a given point, the 2σ value



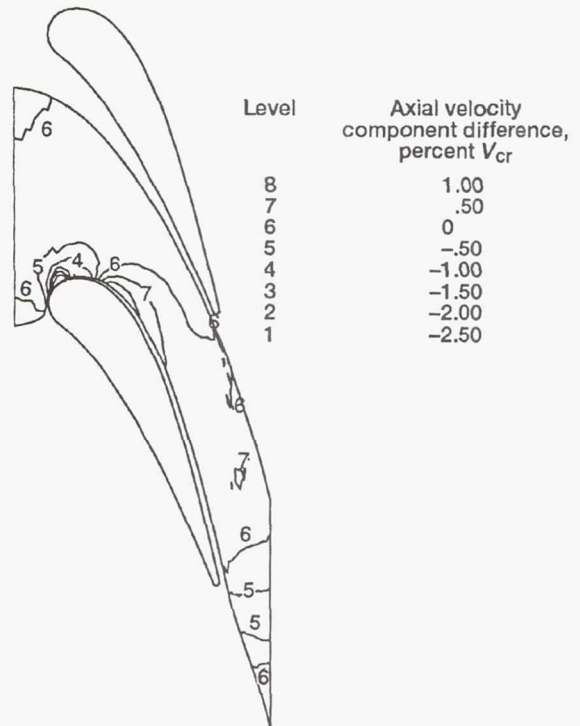
(a) Tangential velocity component difference, $(|V_{\theta,p}| - |V_{\theta,g}|)/V_{cr}$, for 0.5- μm -diameter particles.



(b) Axial velocity component difference, $(|V_{z,p}| - |V_{z,g}|)/V_{cr}$, for 0.5- μm -diameter particles.



(c) Tangential velocity component difference, $(|V_{\theta,p}| - |V_{\theta,g}|)/V_{cr}$, for 1.0- μm -diameter particles.



(d) Axial velocity component difference, $(|V_{z,p}| - |V_{z,g}|)/V_{cr}$, for 1.0- μm -diameter particles.

Figure 8.—Dynamic behavior of seed particles entrained in airflow through vanes at mean radius.

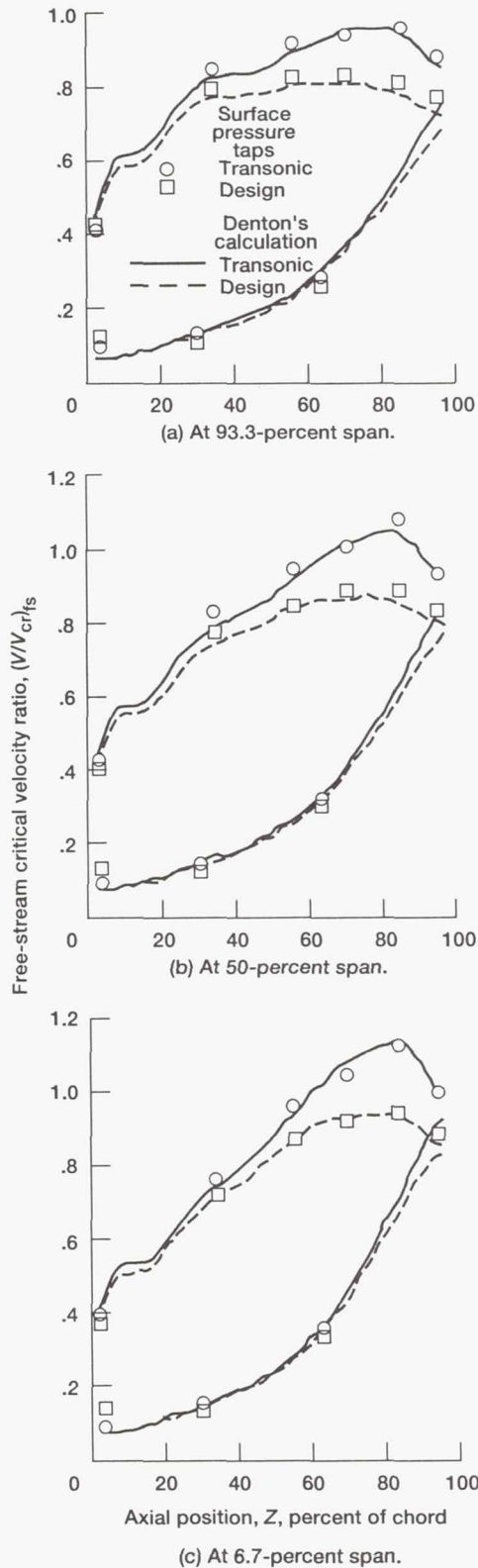


Figure 9.—Comparison of free-stream critical velocity ratio and theory.

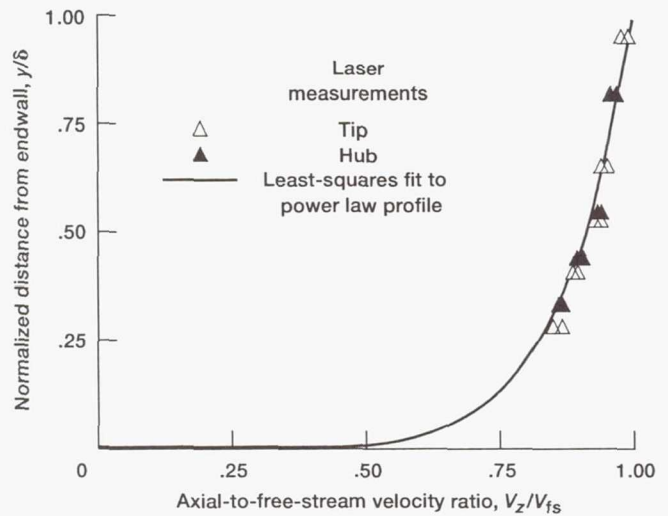


Figure 10.—Radial survey at one axial chord upstream of vanes.

fell within or close to the symbol used to represent the data and was not plotted to avoid confusion in the figures. Similarly, 2σ confidence intervals are not shown when the transonic and design condition results are compared in the same figure. All the confidence interval data are given in tables II and III. Also shown in figures 11 to 15 are the theoretical results obtained from Denton's inviscid flow analysis program. In addition, the circumferential locations of the vane suction and pressure surfaces, which are used in the data presentation figures, are given in table IV.

Upstream Measurements

The laser radial survey measurements, at -100 -percent axial chord, are shown in figure 10. The data from the mean radius to the hub and tip endwalls were each individually least-squares fit to a $1/7$ th power law profile (eq. (6)). This procedure resulted in thicknesses of 8.1 and 9.3 percent of vane height for the tip and hub endwall boundary layers, respectively. Measurements using the LA could be made to about 2 and 3 percent of the tip and hub endwalls, respectively.

The laser circumferential survey results upstream of the vane leading edge are shown in figure 11. The projection of the vane leading edge to the survey plane, shown in this figure, was calculated by using the design inlet flow angle of 0° . In figures 11(a) and (b) for axial positions of -100 - and -50 -percent axial chord, the measurements are compared with the mixed-out value (of the theoretical values at -25 -percent axial chord) because Denton's calculation domain did not extend this far upstream. At these locations the measurements indicate a uniform, axial, inlet velocity. Agreement of the measurements and the mixed-out value is excellent. Comparing the transonic and design flow field

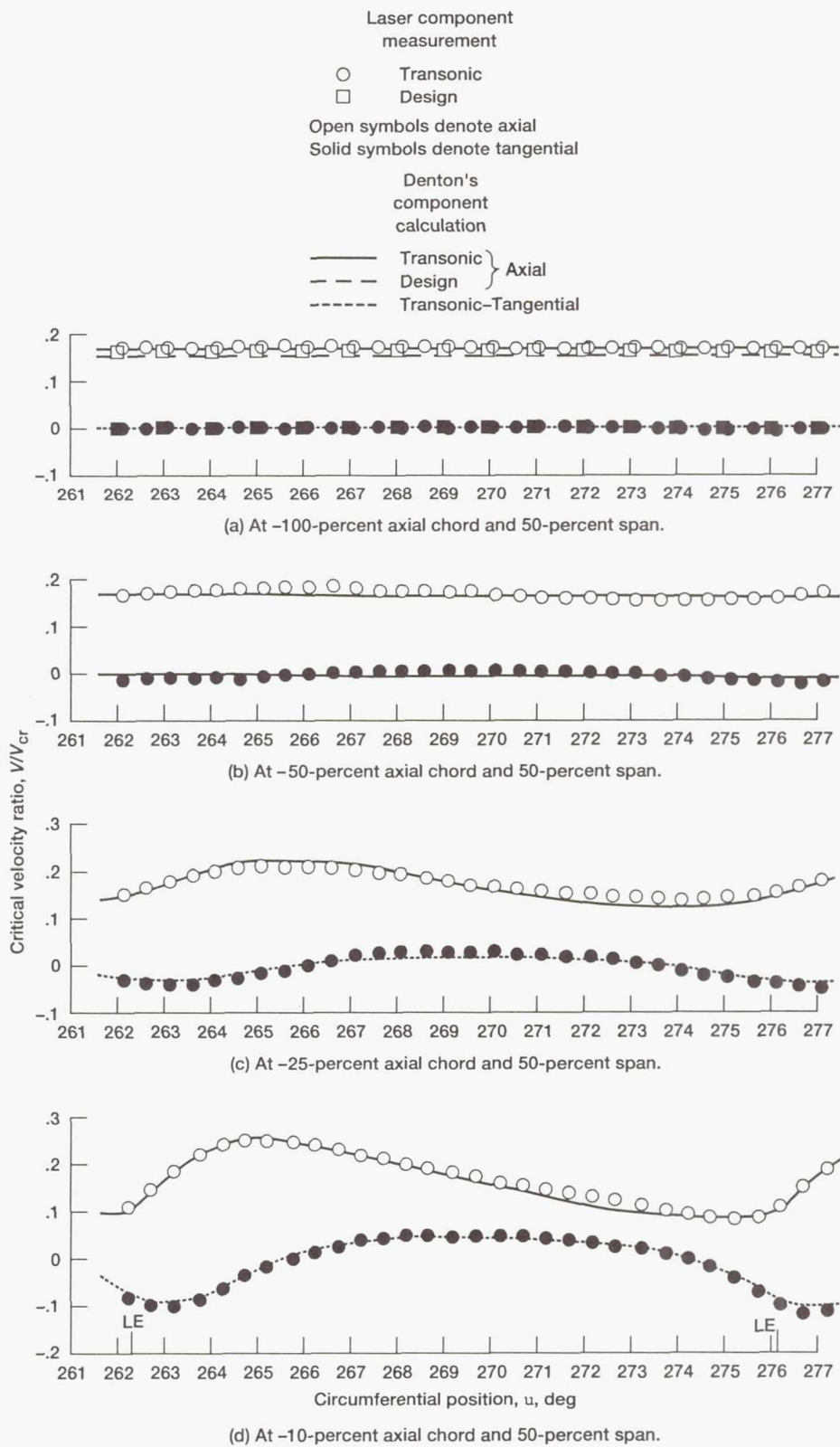


Figure 11.—Comparison of laser measurements and theory upstream of vane leading edge.

results, at -100-percent axial chord (fig. 11(a)), shows only a slight difference in the axial velocity level. At -50-percent axial chord (fig. 11(b)) a slight influence of the vane leading edge appears. At -25- and -10-percent axial chord (figs. 11(c) and (d)) the influence of the leading edge on the measurements is clearly evident. Agreement of the data and the theoretical calculations is also very good to excellent at these positions.

Passage Measurements

Measurements within the vane passage were made at every 10 percent of axial chord from the vane leading edge to the vane trailing edge, and these results are shown in figures 12 to 14. For discussion purposes the passage has been arbitrarily divided into leading-edge, mid-passage, and trailing-edge regions.

Region near vane leading edge.— At 0- to 30-percent axial chord (fig. 12) the substantial velocity changes from suction side to pressure side of the passage are caused by the large flow turning in the leading-edge region. In general, agreement is very good to excellent between the measurements and Denton's calculations. There is no indication of seed particle lag near the suction surface as was indicated in the particle dynamics calculations. At a position of 20-percent axial chord (fig. 12(c)), the transonic and design-condition flow field results show slight differences in the axial component, particularly near the suction surface.

Region near vane mid-passage.— At 40- to 60-percent axial chord (fig. 13) the agreement of the measurements and the calculations is still very good. At 40-percent axial chord (fig. 13(a)), near the suction surface, the measured axial component is somewhat higher than the calculations. This was predicted by the seed particle dynamics calculation (fig. 8). However, although similar behavior was predicted at 50- and 60-percent axial chord, the measurements do not bear this out and agree quite well with Denton's calculations. At 50-percent axial chord (fig. 13(b)), comparing the transonic and design flow results shows some flow field differences in the axial and tangential components, particularly near the suction surface.

Region near vane trailing edge.— At 70- to 100-percent axial chord (fig. 14), the flow turning results in large tangential velocity components. At these positions more statistical uncertainty bars appear in the figures. In addition, the trends in the measurements across the vane passage are not as smooth as at previous survey locations. This region is the most difficult for the laser anemometer measurements, and similar behavior was found previously for the design flow tests. At 90- and 100-percent axial chord multiple sets of measurements were taken on different days, and all the data are shown in figures 14(c) and (d). Some of the largest differences between the measurements and calculations occur in this region, particularly the tangential component near the

suction surface at 80-percent axial chord. In general, the tangential component measurements near the suction surface are lower than theory in this region of the passage. The particle dynamics calculation (fig. 8) did not indicate any significant seed lag problems occurring here. However, the flow in this region is transonic. Any weak oblique shocks and subsequent boundary layer interactions that may occur would not be predicted by Denton's inviscid analysis and therefore are not included in the particle dynamics calculations.

At 80- and 100-percent axial chord (figs. 14(b) and (c)), comparing the transonic and design flow results shows, not unexpectedly, significant flow field differences, particularly in the level of the tangential components.

Downstream Measurements

The results downstream of the vane trailing edge are shown in figure 15. The projection of the vane trailing edge to the survey plane, shown in this figure, was calculated by using the design exit flow angle of 75°. At 105-percent axial chord (fig. 15(a)) the wake from the vane is clearly defined in the tangential component measurements. Outside of the viscous region the agreement between measurements and the inviscid calculations is good, but the tangential component measurements are lower than theory. As the flow proceeds downstream, the wake mixes out and can be less clearly delineated but is still present at 150-percent axial chord (fig. 15(d)). Because the calculation domain did not extend to the 150-percent axial chord location, comparisons were made thereafter with the mixed-out value (of the calculated values at 125-percent axial chord), which tends to be higher than measured. At 175-percent axial chord (fig. 15(e)) the flow is more uniform but still has not completely mixed out. At 150-percent axial chord (fig. 15(d)), comparing the transonic and design flow results shows, as expected, significant flow field differences, particularly in the tangential components.

Turbulence Measurements

The turbulence intensity at each measurement point is presented in tables II and III. These values were obtained from the LA measurements by assuming isotropic turbulence and negligible laser noise, as described in the section Calculation Procedures. Contours of turbulence intensity at the mean radius are shown in figure 16. In general, the turbulence level varies from about 3 to 4 percent upstream of the vanes, 2 to 3 percent in the vane passage, and 3 to 5 percent downstream of the vanes. Within the vane wakes turbulence levels as high as 9 to 10 percent occur near the trailing edge but dissipate rapidly moving downstream. Similar turbulence levels were measured and reported previously for the design flow tests (ref. 8), although the trends were somewhat different.

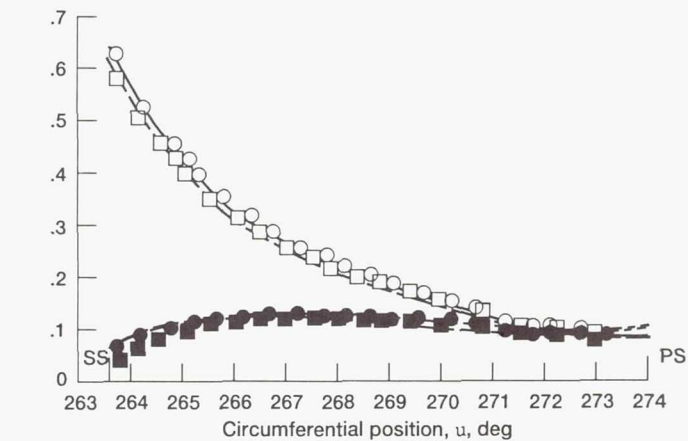
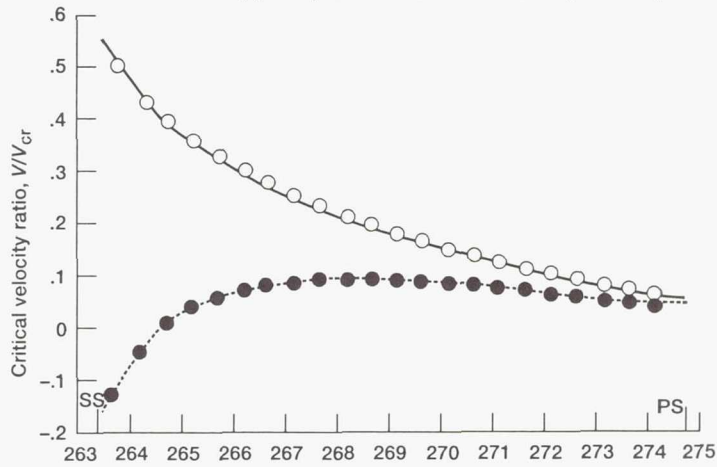
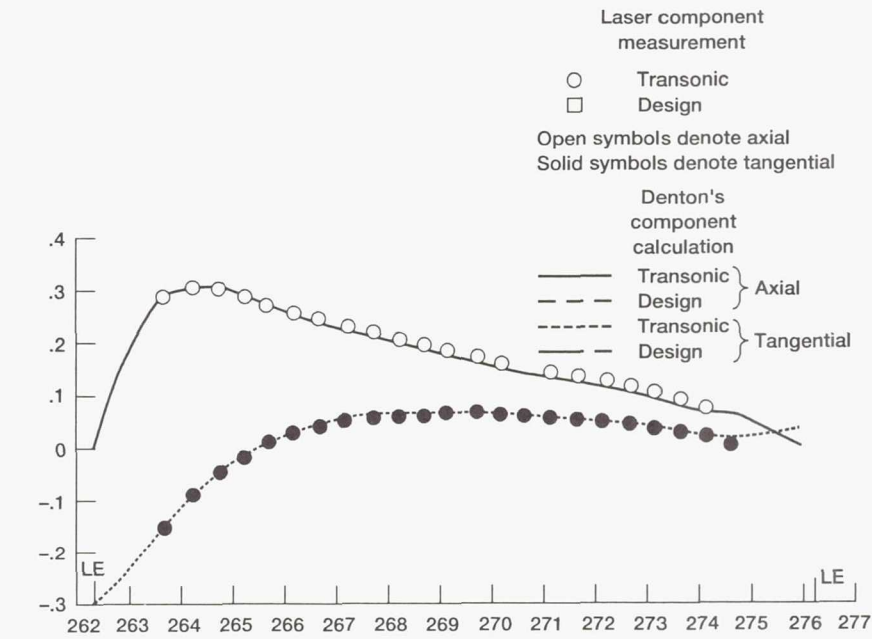


Figure 12.—Comparison of laser measurements and theory within vane passage near leading edge.

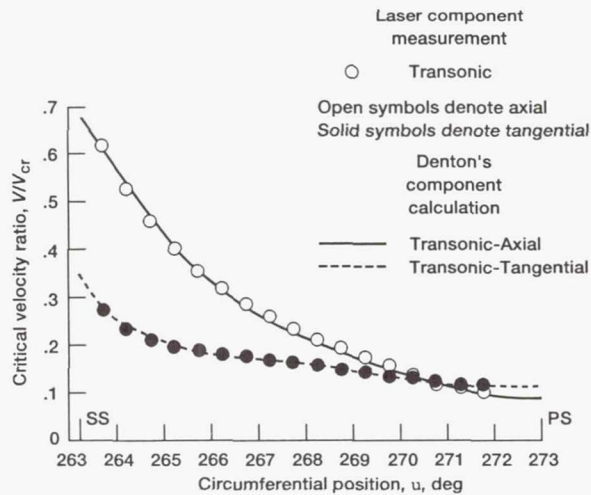


Figure 12.—Concluded.

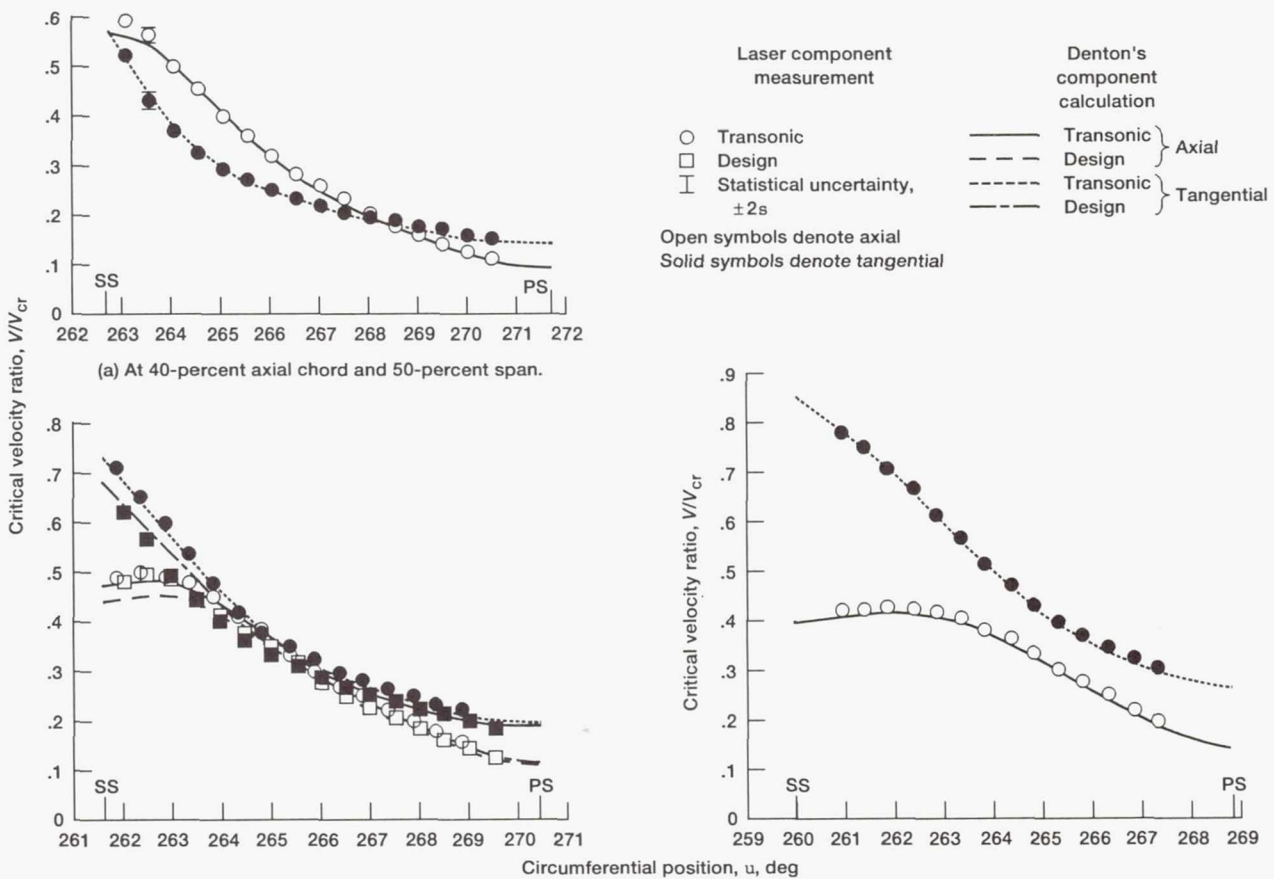


Figure 13.—Comparison of laser measurements and theory within vane passage near midpassage.

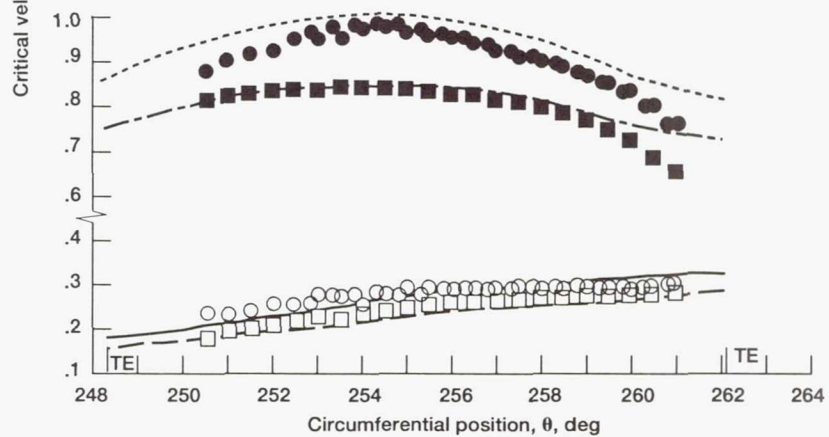
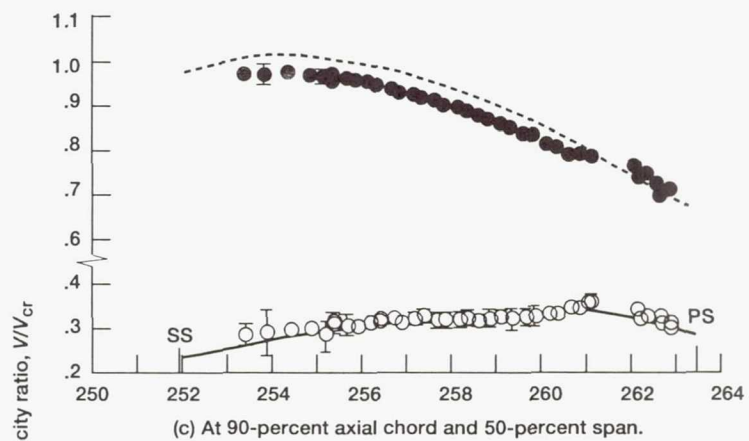
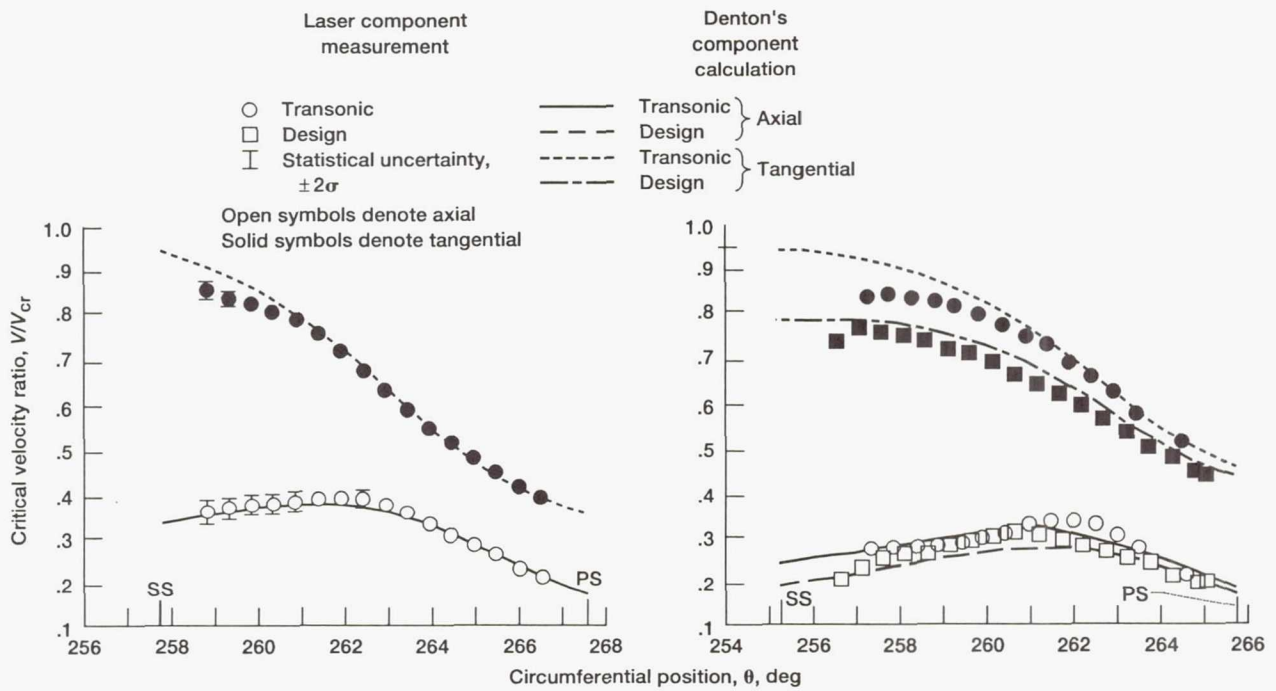


Figure 14.—Comparison of laser measurements and theory within vane passage near trailing edge.

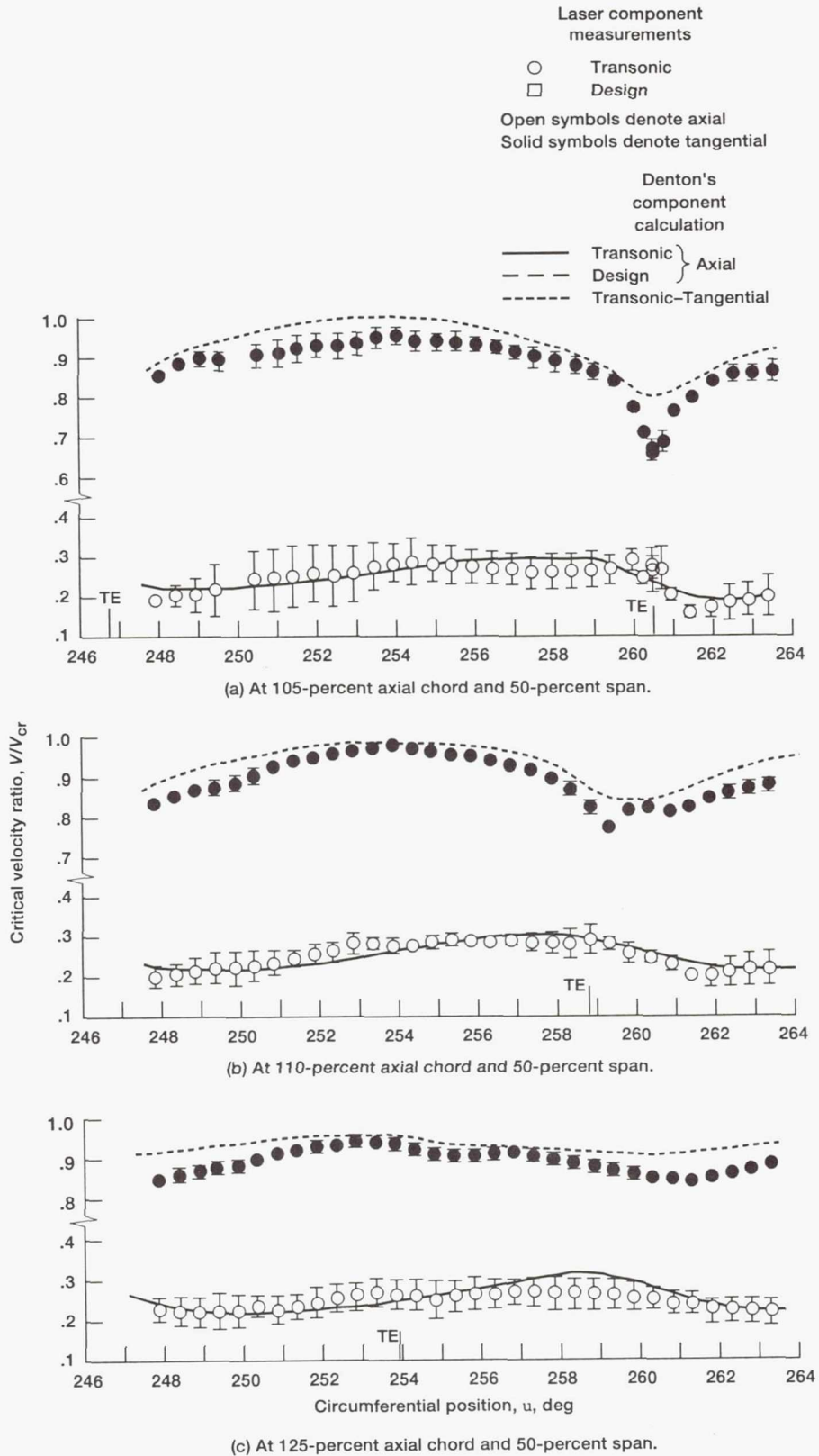
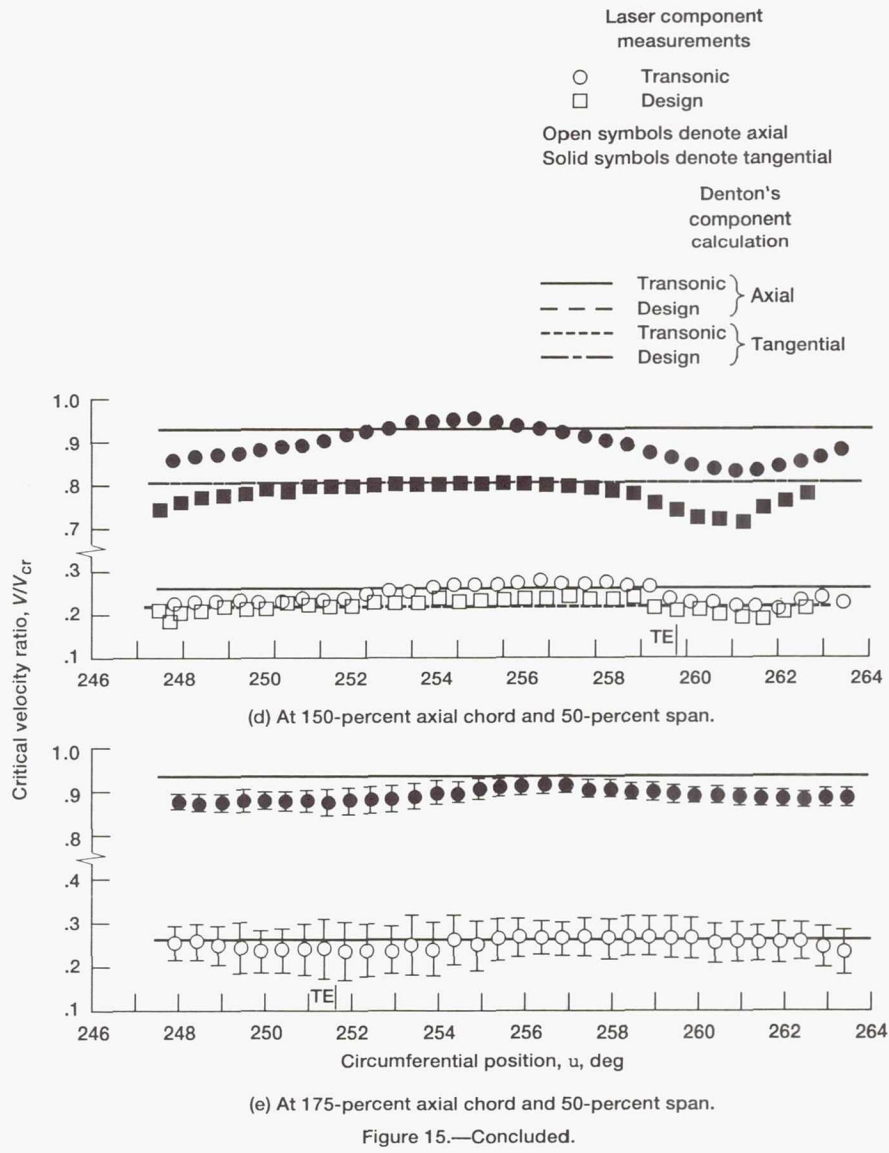


Figure 15.—Comparison of laser measurements and theory downstream of vane trailing edge.



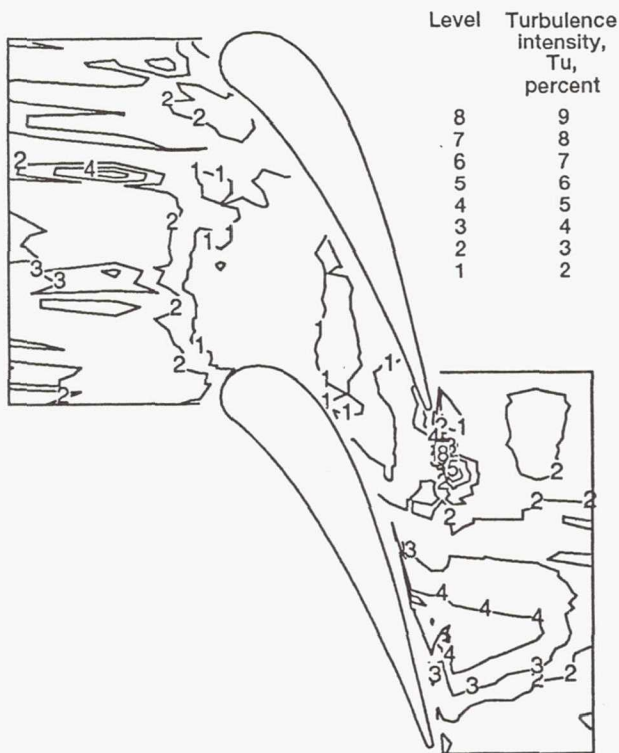


Figure 16.—Laser anemometer measurement of turbulence intensity at mean radius.

Summary of Results

An advanced laser anemometer (LA) was used to measure the mean axial and tangential velocity components in an annular cascade of turbine stator vanes operating at transonic flow conditions. The vanes tested were based on a previous redesign of the first-stage stator in a two-stage turbine for a high-bypass-ratio engine. The vanes produced 75° of flow turning. Tests were conducted on a 0.771-scale model of the engine-sized stator. The advanced LA fringe system employed an extremely small 50- μm -diameter probe volume. This smaller size allowed the laser power to be more concentrated in the probe volume, permitting measurements to be obtained from smaller seed particles and closer to surfaces. Beam correction optics were employed to prevent the beams from uncrossing in passing through the curved optical access window. In addition, the access window was manufactured to the same high quality as the other optical components used in the LA system.

A particle dynamics calculation was performed for this vane geometry and operating condition to determine how well seed particles tracked the airflow. Experimental LA measurements of velocity and turbulence were obtained at the mean radius both upstream of, within, and downstream of

the stator vane row at an exit critical velocity ratio of 1.050 at the hub. In addition, a radial survey was taken at the upstream location to determine the boundary layer thickness. Surface static pressure measurements were also obtained near the vane hub, at midspan, and near the tip. The measurements were compared, where possible, with the results from Denton's three-dimensional inviscid flow analysis program. Comparisons were also made with the results obtained previously when these same vanes were tested at the design exit critical velocity ratio of 0.896 at the hub. The data are presented in both graphical and tabulated form so that they may be readily compared against other turbomachinery computations. The results of this investigation are as follows:

1. Seed particles of 0.5- μm diameter, which represent the bulk of the aerosol generated by the seeder, followed the flow to within ± 0.75 percent (of critical velocity ratio) in both the axial and tangential velocity components. Seed particles of 1- μm diameter, which are near the upper end of the seed particle distribution, generally followed the flow to within ± 1.5 percent (of critical velocity ratio) in both velocity components. However, differences of -2.5 percent in the tangential velocity component were indicated close to the vane suction surface near the leading-edge region.

2. The experimental measurements of vane surface static pressures agreed well with the calculated values. Comparing the transonic and design flow results indicated little difference on the vane pressure surface until about 90-percent axial chord. However, on the vane suction surface the distributions deviated from each other from about 50-percent axial chord until the trailing edge.

3. At the upstream location (-100 -percent axial chord) the laser anemometer measurements indicated that the flow at the mean radius was circumferentially uniform and axial in direction, in accordance with the calculated mixed-out value. Comparing the transonic and design flow measurements with theory showed only slight differences in the axial component levels. In addition, the radial surveys indicated boundary layer thicknesses of 8.1 and 9.3 percent of vane height at the tip and hub endwalls, respectively. Laser anemometer measurements could be made to about 2 and 3 percent (of vane height) at the tip and hub endwalls, respectively.

4. Upstream of the vanes, at -25 - and -10 -percent axial chord, the effect of the vane leading edge was clearly evident, and the agreement between the measurements and the theory was very good to excellent.

5. From the vane leading edge to 60-percent axial chord the agreement between the measurements and the theory was also very good to excellent. From 70-percent axial chord to the vane trailing edge the tangential velocity component measurements were somewhat lower than the calculations, particularly near the vane suction surface. Comparing the transonic and design flow results showed significant differences in the tangential components after the 50-percent axial chord position.

6. The measurements downstream of the vanes but close to the trailing-edge plane clearly indicated the location of the vane wake. The wake deficit dissipated rapidly in moving downstream of the trailing edge and was hard to delineate at 75-percent axial chord downstream of the vanes. Outside the wake regions the measurements agreed reasonably with the inviscid calculations, although the tangential component values were still lower than the calculations. Comparing the transonic and design flow results showed, as expected, significant differences in both the tangential and axial components downstream of the vanes.

7. In general, the turbulence intensity of the flow varied from 3 to 4 percent upstream of the vanes, 2 to 3 percent within the vane passage, and 3 to 5 percent downstream of the vanes. Within the vane wakes turbulence levels as high as 9 to 10 percent were measured.

Lewis Research Center
National Aeronautics and Space Administration
Cleveland, Ohio, March 17, 1993

References

1. Stabe, R.G.; Whitney, W.J.; and Moffitt, T.P.: Performance of a High-Work Low Aspect Ratio Turbine Tested With a Realistic Inlet Radial Temperature Profile. AIAA Paper 84-1161, June 1984. (Also, NASA TM-83655, 1984.)
2. Thulin, R.D.; Howe, D.C.; and Singer, I.D.: Energy Efficient Engine High-Pressure Turbine Detailed Design Report. (PWA-5594-171, Pratt & Whitney Aircraft Group, NASA Contract NAS3-20646), NASA CR-165608, 1982.
3. Halila, E.E.; Lenahan, D.T.; and Thomas, T.T.: Energy Efficient Engine: High Pressure Turbine Test Hardware Detailed Design Report. (R81AEG284, Aircraft Engine Group, General Electric Co., NASA Contract NAS3-20643), NASA CR-167955, 1982.
4. Rangwalla, A.A.; Madavan, N.K.; and Johnson, P.D.: Application of an Unsteady Navier-Stokes Solver to Transonic Turbine Design. AIAA Paper 91-2468, June 1991.
5. Dominy, R.G.; and Harding, S.C.: An Investigation of Secondary Flows in Nozzle Guide Vanes. Secondary Flows in Turbomachines, AGARD CP-469, 1990, pp. 7-1 to 7-15.
6. Horton, G.C.: Secondary Flow Predictions for a Transonic Nozzle Guide Vane. Secondary Flows in Turbomachines, AGARD CP-469, 1990, pp. 8-1 to 8-12.
7. Wegener, D.; Quest, J.; and Hoffmann, W.: Secondary Flow in a Turbine Guide Vane With Low Aspect Ratio. Secondary Flows in Turbomachines, AGARD CP-469, 1990, pp. 9-1 to 9-9.
8. Goldman, L.J.; and Seasholtz, R.G.: Laser Anemometer Measurements and Computations in an Annular Cascade of High Turning Core Turbine Vanes. NASA TP-3252, 1992.
9. Denton, J.D.: An Improved Time Marching Method for Turbomachinery Flow Calculation. J. Eng. Power, vol. 105, no. 3, July 1983, pp. 514-524. (Also, ASME Paper 82-GT-239, 1982.)
10. Goldman, L.J.; and Seasholtz, R.G.: Laser Anemometer Measurements in an Annular Cascade of Core Turbine Vanes and Comparison With Theory. NASA TP-2018, 1982.
11. Goldman, L.J.; and Seasholtz, R.G.: Three Component Laser Anemometer Measurements in an Annular Cascade of Core Turbine Vanes With Contoured End Wall. NASA TP-2846, 1988.
12. Wernet, M.P.; and Seasholtz, R.G.: Zoom Lens Compensator for a Cylindrical Window in Laser Anemometer Uses. Appl. Opt., vol. 26, no. 21, Nov. 1, 1987, pp. 4603-4611.
13. Goldman, L.J.; and Seasholtz, R.G.: Comparison of Laser Anemometer Measurements and Theory in an Annular Turbine Cascade With Experimental Accuracy Determined by Parameter Estimation. Engineering Applications of Laser Velocimetry, H.W. Coleman and P.A. Pfund, eds., ASME, 1982, pp. 83-92. (Also, NASA TM-82860, 1982.)
14. Maxwell, B.R.: Particle Flow in Turbomachinery With Application to Laser-Doppler Velocimetry. AIAA J., vol. 12, no. 10, Oct. 1974, pp. 1297-1298.

TABLE I. — VANE SURFACE STATIC PRESSURE MEASUREMENTS FOR HIGH TURNING CORE TURBINE STATOR AT TRANSONIC FLOW CONDITIONS

Radial position, R, percent	Axial position, Z, percent	Suction surface pressure ratio, P_{ss}/P_0	Pressure surface pressure ratio, P_{ps}/P_0
6.7	2.65	0.915	-----
	34.44	.705	-----
	56.58	.562	-----
	71.11	.500	-----
	85.43	.442	-----
	96.29	.533	-----
	3.30	-----	0.996
	30.29	-----	.989
	63.76	-----	.932
	50.0	2.65	0.903
34.44		.657	-----
56.58		.574	-----
71.11		.527	-----
85.43		.472	-----
96.29		.581	-----
3.30		-----	0.996
30.29		-----	.989
63.76		-----	.943
93.3		2.65	0.901
	34.44	.636	-----
	56.58	.587	-----
	71.11	.567	-----
	85.43	.555	-----
	96.29	.614	-----
	3.30	-----	0.994
	30.29	-----	.990
	63.76	-----	.952

TABLE II. — LASER ANEMOMETER MEASUREMENTS ONE AXIAL CHORD UPSTREAM OF HIGH TURNING CORE TURBINE STATOR VANE AT TRANSONIC FLOW CONDITIONS
[Axial position, Z, -100 percent.]

Radial position, R, percent	Axial velocity ratio, V_z/V_{cr}	Standard deviation, σ/V_{cr}	Circumferential velocity ratio, V_θ/V_{cr}	Standard deviation, σ/V_{cr}	Turbulence intensity, Tu, percent
97.80	0.146	0.001	0.002	0.003	9.9
97.80	.149	.002	.003	.005	9.1
96.81	.154	.002	.002	.006	7.8
96.81	.153	.001	.007	.002	8.3
95.81	.160	.002	.008	.005	6.4
95.81	.162	.001	.001	.002	6.1
94.81	.164	↓	.001	.003	5.3
94.81	.162	↓	-.002	.003	5.7
92.35	.171	↓	.009	.002	3.6
92.35	.169	↓	.005	.002	3.6
89.82	.172	↓	.002	.002	3.2
89.82	.172	0	-.001	.001	2.7
74.85	.173	0	.003	↓	2.3
74.85	↓	.001	.006	↓	2.2
49.90	↓	0	.002	↓	1.8
↓	↓	↓	.003	↓	2.0
↓	↓	↓	.003	↓	1.8
24.95	↓	↓	.004	0	1.7
24.95	↓	↓	.001	.001	1.7
24.95	↓	↓	.003	.001	1.6
9.98	.171	.001	.005	.002	2.8
9.98	.172	0	.005	.001	1.9
7.52	.166	.001	.002	.004	4.7
7.52	.165	.002	.002	.005	5.3
4.99	.161	.001	.003	.003	5.6
4.99	.162	.001	.001	.004	5.5
3.99	.156	.001	.004	↓	7.0
3.99	.154	.002	-.001	↓	7.6
2.99	.149	.002	-.005	↓	8.6
2.99	.148	.002	.006	.005	9.8

TABLE III. — LASER ANEMOMETER MEASUREMENTS FOR HIGH TURNING CORE TURBINE STATOR VANE AT TRANSONIC FLOW CONDITIONS

Axial position, Z, percent	Radial position, R, percent	Tangential position, θ , deg	Axial velocity ratio, V_z/V_{cr}	Standard deviation, σ/V_{cr}	Circumferential velocity ratio, V_θ/V_{cr}	Standard deviation, σ/V_{cr}	Turbulence intensity, Tu, percent	
-100.0	50.0	262.15	0.173	0	0.001	0.001	2.7	
		262.65	.174	0	-.001	.001	2.4	
		263.15	.173	.001	0	.002	4.6	
		263.65	.173	.001	-.002	.003	5.0	
		264.15	.174	0	-.001	.001	3.2	
		264.65		.001	-.002	.002	4.2	
		265.15	↓	.001	0	.001	3.6	
		265.65	↓	.001	0	.002	3.3	
		266.15	.175	0	.002	.001	3.8	
		266.65	.174		.001		3.8	
		267.15	↓		0		3.3	
		267.65			.002		3.6	
		268.15	↓		.001		2.8	
		268.65	↓		.002		2.9	
		269.15	.173		0		2.8	
		269.65	.173		.003	.001	2.9	
		270.15	.172		.002	.001	3.0	
		270.65	.172	↓	0	.001	3.0	
		271.15	.172		.001	.003	3.3	
		271.65	.171		.001	.002	2.8	
		272.15	↓		.001	-.001	.001	2.7
		272.65	↓		0	.001		2.9
		273.15	↓			.001		2.9
		273.65	↓			-.001		3.1
		274.15	.170	↓		0		3.1
		274.65	.171	.001		-.003	.002	3.0
		275.15	.171	0		-.003	.001	2.9
275.65	.172	.001		0		3.0		
276.15	.173	0		-.003		3.6		
276.65	.172	0		0		3.5		
277.15	.173	0		-.001	↓	2.8		
-50.0	50.0	262.15	0.167	0.001	-0.012	0.002	3.6	
		262.65	.171	.001	-.010	.002	3.3	
		263.15	.174	0	-.010	.001	3.3	
		263.65	.178	0	-.011	.001	3.5	
		264.15	.181	0	-.008	.001	3.8	
		264.65	.183	.001	-.010	.002	3.5	
		265.15	.184		-.006	.002	3.6	
		265.65	.187		-.002	.002	3.8	
		266.15	.187		.003	.001	4.5	
		266.65	.187		.003	.003	3.5	
		267.15	.185		.007	.002	4.8	
		267.65	.182		.009	.002	5.2	
		268.15	.181	↓	.008	.002	3.5	
		268.65	.180	0	.009	.001	3.6	
		269.15	.177	.001	.010	.002	3.9	
		269.65	.173	.001	.010	.001	3.4	
		270.15	.171	0	.012	.001	3.6	
		270.65	.168	.001	.012	.002	3.9	
		271.15	.167		.008		3.1	
		271.65	.163		.009		5.7	
272.15	.163		.006	↓	2.8			
272.65	.161		.004	.001	2.9			
273.15	.160		.004	.001	3.2			
273.65	.160	↓		-.001	.002	2.5		

TABLE III. — Continued.

Axial position, Z, percent	Radial position, R, percent	Tangential position, θ , deg	Axial velocity ratio, V_z/V_{cr}	Standard deviation, σ/V_{cr}	Circumferential velocity ratio, V_θ/V_{cr}	Standard deviation, σ/V_{cr}	Turbulence intensity, Tu, percent
-50.0	50.0	274.15	0.161	0.001	-0.002	0.002	3.0
		274.65	.162	.001	-.007	.002	2.5
		275.15	.164	.001	-.009	.002	2.7
		275.65	.166	0	-.010	.001	3.5
		276.15	.169	.001	-.013	.002	2.8
		276.65	.173	.001	-.014	.002	3.2
		277.15	.176	.001	-.012	.002	3.7
-25.0	50.0	262.15	0.153	0	0.035	0.001	3.2
		262.65	.164	0	-.039	.001	3.8
		263.15	.178	.001	-.042	.002	3.4
		263.65	.191	0	-.042	.001	3.4
		264.15	.201	.001	-.034	.002	3.6
		264.65	.206	.001	-.028	.002	3.3
		265.15	.210	0	-.017	.001	3.0
		265.65	.211	0	-.009	.001	2.7
		266.15	.210	.001	.001	.002	3.4
		266.65	.207	.001	.011	.002	3.8
		267.15	.204	.001	.022	.004	2.5
		267.65	.199	0	.025	.001	2.8
		268.15	.193	.001	.028	.002	3.2
		268.65	.187	.001	.029	.001	3.0
		269.15	.182	0	.029	0	3.1
		269.65	.175	.001	.027	.002	3.2
		270.15	.169		.028	.001	3.5
		270.65	.164		.021	.003	3.4
		271.15	.158		.022	.002	2.5
		271.65	.153		.021	.002	2.8
		272.15	.150		.017		2.7
		272.65	.145		.015		3.0
		273.15	.143		.008		2.6
		273.65	.140		.002		2.9
		274.15	.138	0	-.009	.001	2.9
		274.65	.139	.001	-.018	.002	3.0
		275.15	.143	0	-.024	.001	2.5
275.65	.148	.001	-.033	.002	2.7		
276.15	.157	.001	-.035	.002	4.6		
276.65	.169	.001	-.043	.002	3.7		
277.15	.183	0	-.046	.001	3.7		
-10.0	50.0	262.20	0.110	0.001	-0.087	0.002	2.7
		262.70	.144	.001	-.105	.002	3.5
		263.20	.188		-.105	.001	3.7
		263.70	.222		-.089	.002	2.3
		264.20	.245		-.069	.002	2.5
		264.70	.254		-.040	.001	1.6
		265.20	.254		-.020	.003	1.8
		265.70	.251	0	-.004	.001	1.8
		266.20	.244	.001	-.011	.003	1.8
		266.70	.234		.022	.003	1.5
		267.20	.223		.037	.003	1.5
		267.70	.215		.041	.004	1.5
		268.20	.205		.049	.002	1.6
		268.70	.196		.049	.002	1.8
		269.20	.187		.047	.001	1.8
269.70	.176		.050	.002	2.2		

TABLE III. — Continued.

Axial position, Z, percent	Radial position, R, percent	Tangential position, θ , deg	Axial velocity ratio, V_z/V_{cr}	Standard deviation, σ/V_{cr}	Circumferential velocity ratio, V_θ/V_{cr}	Standard deviation, σ/V_{cr}	Turbulence intensity, Tu, percent
-10.0	50.0	270.20	0.166	0.001	0.050	0.001	2.4
		270.70	.157	↓	.050	.001	2.0
		271.20	.150	↓	.045	.002	2.0
		271.70	.143	↓	.040	↓	1.9
		272.20	.137	↓	.033	↓	2.6
		272.70	.130	↓	.025	↓	3.0
		273.20	.120	0	.021	.001	2.7
		273.70	.113	.001	.013	↓	2.8
		274.20	.105	0	.002	↓	3.4
		274.70	.097	.001	-.013	↓	3.1
		275.20	.093	0	-.037	↓	3.6
		275.70	.098	.001	-.066	↓	2.3
		276.20	.121	.001	-.096	↓	2.1
		276.70	.160	.001	-.114	.002	2.1
277.20	.199	.002	-.106	.003	1.6		
0	50.0	263.70	0.300	0.002	-0.153	0.003	1.6
		264.20	.318	.001	-.088	.002	1.5
		264.70	.313	↓	-.044	.002	1.6
		265.20	.299	↓	-.012	.003	1.5
		265.70	.284	↓	.017	.004	1.3
		266.20	.268	0	.035	.001	1.7
		266.70	.254	0	.043	.001	1.8
		267.20	.239	.001	.054	.002	1.8
		267.70	.225	0	.060	.001	2.1
		268.20	.212	.001	.063	.003	1.8
		268.70	.200	.001	.065	.003	2.3
		269.20	.187	.001	.070	.001	2.1
		269.70	.176	0	.070	.001	2.6
		270.20	.163	.001	.067	.001	2.0
		270.70	.153	.001	.063	.002	1.9
		271.20	.144	.001	.061	.001	1.9
		271.70	.135	0	.057	.001	2.2
		272.20	.124	0	.052	0	2.4
		272.70	.114	.001	.046	.001	2.5
		273.20	.105	.001	.039	.001	2.7
273.70	.094	0	.032	0	3.3		
274.20	.080	.001	.023	.001	4.5		
274.70	.065	0	.009	0	5.6		
10.0	50.0	263.65	0.503	0.001	-0.137	0.003	1.6
		264.15	.437	.001	-.048	.002	1.4
		264.65	.392	0	.004	.001	1.4
		265.15	.356	.001	.036	.002	1.2
		265.65	.325	0	.056	.001	1.2
		266.15	.297	.001	.070	.002	1.6
		266.65	.274	.001	.079	.003	1.2
		267.15	.254	0	.085	.001	1.5
		267.65	.235	0	.089	.001	1.5
		268.15	.217	0	.091	0	1.6
		268.65	.201	.001	.091	.001	1.6
		269.15	.186	↓	.093	.002	1.6
		269.65	.173	↓	.090	.002	1.9
		270.15	.160	↓	.088	.002	1.8
		270.65	.147	0	.084	.001	2.1
271.15	.136	.001	.080	.001	2.1		

TABLE III. — Continued.

Axial position, Z, percent	Radial position, R, percent	Tangential position, θ , deg	Axial velocity ratio, V_z/V_{cr}	Standard deviation, σ/V_{cr}	Circumferential velocity ratio, V_θ/V_{cr}	Standard deviation, σ/V_{cr}	Turbulence intensity, Tu, percent
10.0	50.0	271.65	0.126	0.001	0.075	0.001	2.3
		272.15	.117	↓	.069	↓	2.7
		272.65	.103		.065		2.9
		273.15	.093		.059		3.3
		273.65	.081	↓	.053	↓	3.7
		274.15	.067	0	.048	0	3.4
20.0	50.0	263.70	0.624	0.001	0.058	0.002	1.2
		264.20	.522	.001	.080	.001	1.3
		264.70	.449	↓	.095	.001	1.3
		265.20	.392		.112	.002	1.5
		265.70	.351		.114	.002	1.4
		266.20	.316		.120	.002	1.4
		266.70	.289		.119	.001	1.4
		267.20	.257		.129	.002	1.6
		267.70	.239		.121	.001	1.5
		268.20	.219		.121	.001	1.6
		268.70	.199		.117	.001	1.8
		269.20	.181		.117	.002	1.6
		269.70	.168	↓	.114	.001	1.6
		270.20	.153	.002	.110	.003	2.1
		270.70	.140	.001	.103	.001	2.0
		271.20	.126	.001	.101	.001	1.9
		271.70	.115	.002	.096	.002	2.0
		272.20	.104	.002	.090	.002	2.6
272.70	.092	.001	.084	.001	2.3		
273.20	.081	0	.080	0	2.6		
30.0	50.0	263.70	0.618	0.002	0.269	0.002	1.8
		264.20	.526	.001	.231	.001	1.6
		264.70	.459	.001	.210	.002	1.5
		265.20	.401	0	.199	.001	1.5
		265.70	.355	.001	.191	.001	1.4
		266.20	.318	.002	.182	.002	1.4
		266.70	.284	.001	.179	↓	1.4
		267.20	.259	.001	.171		1.5
		267.70	.231	.002	.167	↓	1.5
		268.20	.211	.001	.162	.001	1.6
		268.70	.193	.002	.149	.003	1.6
		269.20	.173	.001	.146	.001	1.8
		269.70	.157	↓	.141	.001	1.5
		270.20	.141		.136	.002	1.7
		270.70	.126		.130	.001	1.7
271.20	.115		.120	.001	1.9		
271.70	.102	↓	.116	.001	2.2		
40.0	50.0	263.00	0.593	0.005	0.521	0.005	1.4
		263.50	.562	.008	.427	.009	1.7
		264.00	.501	.001	.369	.002	1.6
		264.50	.451	.002	.325	.003	1.5
		265.00	.402	.002	.295	.002	1.6
		265.50	.358	.001	.271	.002	1.6
		266.00	.321	↓	.251	.001	1.6
		266.50	.289		.234	.001	1.5
		267.00	.260	↓	.224	.002	1.7
267.50	.234	.003	.210	.003	1.5		

TABLE III. — Continued.

Axial position, Z, percent	Radial position, R, percent	Tangential position, θ , deg	Axial velocity ratio, V_z/V_{cr}	Standard deviation, σ/V_{cr}	Circumferential velocity ratio, V_θ/V_{cr}	Standard deviation, σ/V_{cr}	Turbulence intensity, Tu, percent
40.0	50.0	268.00	0.208	0.002	0.201	0.002	1.7
		268.50	.185	.001	.194	.001	1.5
		269.00	.169	.003	.181	.003	1.7
		269.50	.149	.002	.174	.001	1.7
		270.00	.133	.002	.165	.002	1.6
		270.50	.120	.001	.157	.001	1.5
		50.0	50.0	261.85	0.489	0.006	0.710
262.35	.499			.005	.649	.004	1.4
262.85	.489			.002	.598	.002	2.0
263.35	.476			.003	.534	.002	2.2
263.85	.448			.005	.475	.004	2.3
264.35	.415			.004	.418	.004	2.5
264.85	.380			.003	.377	.002	2.2
265.35	.342			.002	.348	.001	2.1
265.85	.307			.002	.321		2.0
266.35	.278			.001	.299	↓	2.1
266.85	.249			.002	.282	↓	2.0
267.35	.225			↓	.264	.002	2.0
267.85	.201			↓	.249	.002	2.1
268.35	.179			↓	.233	.002	2.3
268.85	.157	.001	.222	.001	2.0		
60.0	50.0	260.85	0.425	0.007	0.784	0.004	1.9
		261.35	.425	.005	.754	.003	1.8
		261.85	.430	.003	.712	.002	2.8
		262.35	.428	.002	.667	.001	2.0
		262.85	.422	.003	.617	.002	2.0
		263.35	.407	.004	.568	.003	2.1
		263.85	.392	.007	.514	.005	2.2
		264.35	.364	.004	.470	.003	2.3
		264.85	.334	.003	.432	.002	2.3
		265.35	.303	.001	.400	0	2.2
		264.85	.274	.002	.370	.001	2.1
		266.35	.248	.001	.345	.001	2.1
		266.85	.221	.002	.326	.001	2.2
		267.35	.197	.001	.305	0	1.9
70.0	50.0	258.85	0.362	0.015	0.859	0.009	2.4
		259.35	.372	.013	.843	.007	2.3
		259.85	.378	.010	.831	.006	1.9
		260.35	.382	.012	.812	.007	1.9
		260.85	.386	.010	.790	.006	1.7
		261.35	.391	.005	.759	.003	1.6
		261.85	.395	.004	.722	.002	1.7
		262.35	.395	.009	.677	.005	1.8
		262.85	.377	.007	.634	.004	1.8
		263.35	.358	.005	.591	.003	1.9
		263.85	.330	.004	.553	.002	1.8
		264.35	.306	.003	.518	.002	1.7
		264.85	.282	.003	.487	.002	1.6
		265.35	.265	.002	.453	.001	1.6
265.85	.229	.003	.416	.002	1.5		
266.35	.207	.002	.393	.001	1.4		

TABLE III. — Continued.

Axial position, Z, percent	Radial position, R, percent	Tangential position, θ , deg	Axial velocity ratio, V_z/V_{cr}	Standard deviation, σ/V_{cr}	Circumferential velocity ratio, V_θ/V_{cr}	Standard deviation, σ/V_{cr}	Turbulence intensity, Tu, percent
80.0	50.0	257.35	0.324	0.034	0.882	0.017	3.7
		257.85	.324	.028	.884	.014	2.9
		258.35	.327	.025	.875	.013	2.3
		258.85	.329	.029	.860	.015	1.9
		259.35	.331	.026	.849	.013	1.9
		259.85	.340	.022	.834	.011	1.9
		260.35	.349	.017	.817	.009	1.8
		260.85	.367	.014	.795	.007	1.8
		261.35	.375	.008	.772	.004	1.8
		261.85	.376	.011	.738	.006	2.0
		262.35	.367	.011	.701	.005	2.2
		262.85	.343	.011	.661	.005	2.3
		263.35	.316	.005	.619	.003	2.1
		264.35	.257	.003	.553	.002	1.4
90.0	50.0	255.25	0.281	0.017	0.962	0.008	4.0
		255.75	.310	.009	.954	.005	3.0
		256.25	.313	.006	.949	.003	2.9
		256.75	.323	.006	.930	.003	2.6
		257.25	.316	.008	.919	.004	2.5
		257.75	.316	.009	.904		2.6
		258.25	.316	.008	.892	↓	3.0
		258.75	.319	.008	.870	↓	2.7
		259.25	.322	.008	.850	↓	2.5
		259.75	.320	.007	.829	.003	2.4
		260.25	.330	.006	.805	.003	2.4
		260.75	.347	.004	.780	.002	2.5
		261.25	.357	.004	.774	.002	2.2
		262.25	.319	.006	.732	.003	1.9
262.75	.304	.007	.694	.004	2.3		
90.0	50.0	255.45	0.313	0.012	0.950	0.006	3.2
		255.95	.305	.005	.950	.003	2.7
		256.45	.315	.005	.937	.002	2.9
		256.95	.313	.004	.923	.002	2.5
		257.45	.321	.008	.907	.004	2.5
		257.95	.319	.008	.894	↓	2.3
		258.45	.320	.008	.880	↓	2.4
		258.95	.319	.009	.864	↓	2.3
		259.45	.320	.011	.844	.005	
		259.95	.322	.009	.823	.005	↓
		260.45	.329	.007	.799	.003	↓
		260.95	.344	.005	.778	.003	2.4
		262.45	.319	.007	.735	.004	2.1
		262.95	.297	.007	.699	.003	2.2
90.0	50.0	253.45	0.287	0.013	0.970	0.006	4.8
		253.95	.292	.025	.966	.012	6.5
		254.45	.297	.004	.972	.002	4.3
		254.95	.299	.006	.966	.003	4.1
		255.45	.304	.005	.962	.002	4.2
		255.95	.305	.005	.954	.002	3.9
		256.45	.311	.005	.939	.002	3.6
		256.95	.313	.005	.926	.003	3.2

TABLE III. — Continued.

Axial position, Z, percent	Radial position, R, percent	Tangential position, θ , deg	Axial velocity ratio, V_z/V_{cr}	Standard deviation, σ/V_{cr}	Circumferential velocity ratio, V_θ/V_{cr}	Standard deviation, σ/V_{cr}	Turbulence intensity, Tu, percent
90.0	50.0	257.45	0.321	0.008	0.910	0.004	3.0
		257.95	.318	.010	.895	.005	3.0
		258.45	.320	.009	.880	.004	2.9
		258.95	.316	.010	.864	.005	2.9
		259.45	.318	.012	.846	.006	2.3
		259.95	.323	.011	.825	.005	2.5
		260.45	.330	.005	.800	.003	2.6
		260.95	.341	.005	.783	.003	2.5
		261.20	.354	.009	.775	.004	2.7
		262.20	.338	.007	.751	.003	2.2
		262.45	.320	.005	.736	.003	2.0
		262.70	.326	.006	.715	.003	2.8
		262.95	.304	.005	.703	.002	2.7
		100.0	50.0	252.85	0.266	0.020	0.971
253.35	.283			.012	.982	.005	4.8
253.85	.284			.015	.983	.007	4.2
254.35	.290			.009	.987	.004	4.6
254.85	.285			.009	.985	.004	4.3
255.35	.286			.005	.975	.002	3.7
255.85	.296			.006	.963	.003	3.6
256.35	.296			.004	.951	.002	3.2
256.85	.295			.004	.936	.002	3.2
257.35	.293			.006	.923	.003	3.3
257.85	.300			.008	.908	.003	3.1
258.35	.295			.007	.893	.003	2.9
258.85	.297			.008	.874	.004	3.2
259.35	.294			.008	.854	.004	3.0
259.85	.292			.006	.831	.003	2.9
260.35	.293			.005	.798	.002	3.1
260.85	.296			.004	.757	.002	4.1
100.0	50.0	250.50	0.244	0.037	0.879	0.016	4.1
		251.00	.239	.035	.902	.015	3.9
		251.50	.246	.028	.917	.012	4.9
		252.00	.266	.026	.920	.011	5.3
		252.50	.265	.013	.951	.006	5.9
		253.00	.284	.012	.952	.005	6.0
		253.50	.280	.008	.954	.004	5.8
		254.00	.259	.007	.977	.003	5.1
		254.50	.286	.004	.981	.002	4.2
		255.00	.303	.004	.965	.002	4.0
		255.50	.301	.003	.960	.001	3.7
		256.00	.296	.005	.951	.002	3.2
		256.50	.300	.005	.938	.002	3.1
		257.00	.296	.008	.924	.004	3.1
		257.50	.298	.011	.908	.005	2.8
		258.00	.291	.010	.901	.004	3.2
		258.50	.291	.011	.886	.005	3.1
		259.00	.292	.013	.868	.006	2.9
		259.50	.291	.012	.851	.005	2.7
260.00	.287	.011	.829	.005	2.6		
260.50	.291	.009	.800	.004	2.8		
261.00	.292	.007	.760	.003	4.6		

TABLE III. — Continued.

Axial position, Z, percent	Radial position, R, percent	Tangential position, θ , deg	Axial velocity ratio, V_z/V_{cr}	Standard deviation, σ/V_{cr}	Circumferential velocity ratio, V_θ/V_{cr}	Standard deviation, σ/V_{cr}	Turbulence intensity, Tu, percent
105.0	50.0	248.00	0.180	0.005	0.839	0.002	1.9
		248.50	.194	.013	.865	.006	1.7
		249.00	.195	.019	.878	.008	2.1
		249.50	.208	.032	.880	.014	3.0
		250.50	.237	.036	.892	.016	3.1
		251.00	.241	.041	.899	.018	3.5
		251.50	.246	.038	.912	.017	3.8
		252.00	.255	.036	.921	.016	4.1
		252.50	.252	.039	.920	.017	3.9
		253.00	.257	.035	.928	.015	4.7
		253.50	.275	.029	.944	.013	5.7
		254.00	.283	.024	.950	.010	5.3
		254.50	.289	.028	.937	.012	5.0
		255.00	.284	.022	.939	.010	5.1
		255.50	.283	.024	.932	.011	4.0
		256.00	.279	.021	.930	.009	3.6
		256.50	.277	.020	.924	.009	3.5
		257.00	.277	.019	.915	.008	3.7
		257.50	.272	.023	.905	.010	3.8
		258.00	.272	.023	.895		3.6
		258.50	.273	.023	.884		2.9
		259.00	.278	.022	.868	▼	2.6
		259.50	.282	.017	.848	.008	2.8
		260.00	.305	.012	.783	.005	5.5
		260.25	.269	.008	.721	.004	9.3
		260.50	.286	.016	.664	.007	10.4
		260.50	.278	.028	.678	.012	10.5
		260.75	.282	.028	.698	.012	10.3
		261.00	.225	.011	.776	.005	5.4
		261.50	.184	.007	.810	.003	2.0
262.00	.191	.014	.851	.006	1.7		
262.50	.203	.023	.868	.010	1.7		
263.00	.209	.022	.871	.010	2.0		
263.50	.221	.027	.878	.012	2.6		
110.0	50.0	247.85	0.198	0.012	0.836	0.005	2.4
		248.35	.207	.014	.856	.006	2.1
		248.85	.215	.015	.870	.007	2.7
		249.35	.225	.018	.875	.008	3.1
		249.85	.221	.021	.888	.009	3.5
		250.35	.225	.020	.905	.009	4.1
		250.85	.236	.014	.926	.006	4.6
		251.35	.247	.013	.941	.006	5.2
		251.85	.261	.011	.950	.005	5.4
		252.35	.260	.012	.960	.005	5.7
		252.85	.287	.012	.965	.005	5.5
		253.35	.284	.008	.968	.003	5.2
		253.85	.278	.011	.977	.005	5.1
		254.35	.279	.006	.971	.003	4.7
		254.85	.287	.009	.965	.004	4.4
		255.35	.295	.008	.955	.004	4.4
		255.85	.288	.006	.951	.002	4.2
		256.35	.287	.006	.940	.003	3.5
		256.85	.290	.009	.928	.004	3.0
		257.35	.286	.012	.914	.005	2.8

TABLE III. — Continued.

Axial position, Z, percent	Radial position, R, percent	Tangential position, θ , deg	Axial velocity ratio, V_z/V_{cr}	Standard deviation, σ/V_{cr}	Circumferential velocity ratio, V_θ/V_{cr}	Standard deviation, σ/V_{cr}	Turbulence intensity, Tu, percent
110.0	50.0	257.85	0.285	0.014	0.896	0.006	2.8
		258.35	.283	.021	.870	.009	3.2
		258.85	.292	.018	.822	.008	4.2
		259.35	.281	.009	.774	.004	6.2
		259.85	.254	.015	.817	.007	5.4
		260.35	.252	.010	.824	.004	2.6
		260.85	.230	.008	.813	.003	2.2
		261.35	.202	.006	.823	.003	1.9
		261.85	.203	.011	.848	.005	1.9
		262.35	.207	.018	.865	.008	2.0
		262.85	.215	.020	.871	.009	2.2
		263.35	.217	.020	.878	.009	2.6
		125.0	50.0	247.90	0.229	0.015	0.848
248.40	.223			.018	.858	.008	2.2
248.90	.222			.018	.866	.008	2.3
249.40	.225			.022	.875	.010	2.5
249.90	.227			.021	.884	.009	2.6
250.40	.237			.014	.898	.006	3.6
250.90	.228			.017	.914	.008	4.3
251.40	.236			.016	.921	.007	4.8
251.90	.245			.019	.931	.008	5.1
252.40	.257			.016	.934	.007	5.4
252.90	.265			.013	.943	.006	5.7
253.40	.271			.016	.940	.007	5.3
253.90	.265			.017	.936	.008	4.9
254.40	.264			.018	.922	.008	4.6
254.90	.250			.023	.911	.010	4.0
255.40	.261			.018	.907	.008	4.2
255.90	.267			.020	.907	.009	4.0
256.40	.265			.018	.915	.008	3.9
256.90	.271			.014	.914	.006	3.4
257.40	.270			.017	.908	.007	3.1
257.90	.267			.022	.895	.010	2.7
258.40	.270			.018	.886	.008	2.3
258.90	.266			.018	.878	.008	2.1
259.40	.264			.018	.870	.008	2.3
259.90	.257			.017	.859	.007	2.3
260.40	.255			.014	.849	.006	2.4
260.90	.244			.015	.846		2.2
261.40	.243	.014	.844		2.2		
261.90	.227	.013	.851		2.3		
262.40	.228	.014	.861	↓	2.3		
262.90	.224	.015	.870	.007	2.5		
263.40	.222	.016	.882	.007	2.6		
150.0	50.0	247.85	0.225	0.020	0.853	0.009	2.9
		248.35	.230	.019	.863	.008	2.5
		248.85	.230	.021	.866	.009	2.6
		249.35	.231	.017	.875	.008	2.4
		249.85	.225	.019	.882	.008	2.5
		250.35	.229	.018	.886	.008	2.8
		250.85	.236	.021	.890	.009	3.0
		251.35	.235	.020	.905	.009	4.0
		251.85	.238	.017	.916	.007	4.6
			.246	.011	.925	.005	4.9

TABLE III. — Concluded.

Axial position, Z, percent	Radial position, R, percent	Tangential position, θ , deg	Axial velocity ratio, V_z/V_{cr}	Standard deviation, σ/V_{cr}	Circumferential velocity ratio, V_θ/V_{cr}	Standard deviation, σ/V_{cr}	Turbulence intensity, Tu, percent
150.0	50.0	252.85	0.253	0.011	0.934	0.005	5.2
		253.35	.250	.008	.945	.004	5.0
		253.85	.264	.011	.943	.005	4.9
		254.35	.266	.010	.950	.004	4.6
		254.85	.264	.009	.950	.004	4.4
		255.35	.269	.010	.944	.004	4.2
		255.85	.272	.011	.935	.005	3.9
		256.35	.276	.010	.927	.004	3.7
		256.85	.270	.012	.921	.005	3.5
		257.35	.269	.019	.911	.008	3.1
		257.85	.273	.017	.902	.007	3.1
		258.35	.264	.022	.887	.010	2.9
		258.85	.269	.027	.871	.012	2.7
		259.35	.236	.018	.862	.008	3.3
		259.85	.227	.012	.847	.005	3.4
		260.35	.225	.014	.836	.006	3.5
		260.85	.220	.011	.831	.005	3.8
		261.35	.217	.018	.833	.008	3.9
		261.85	.214	.017	.843	.008	3.9
		262.35	.236	.013	.848	.006	3.6
262.85	.240	.014	.861	.006	3.0		
263.35	.226	.020	.880	.009	2.6		
175.0	50.0	247.95	0.255	0.020	0.876	0.009	2.2
		248.45	.257	.021	.873	.009	2.0
		248.95	.251	.023	.873	.010	2.0
		249.45	.244	.029	.876	.013	1.9
		249.95	.237	.024	.877	.010	2.2
		250.45	.239	.025	.876	.011	2.3
		250.95	.240	.030	.875	.013	2.4
		251.45	.241	.034	.872	.015	2.3
		251.95	.235	.033	.874	.014	2.3
		252.45	.236	.029	.880	.013	3.2
		252.95	.237	.028	.883	.012	3.3
		253.45	.247	.034	.883	.015	3.2
		253.95	.239	.033	.893	.014	3.6
		254.45	.258	.028	.893	.012	3.8
		254.95	.247	.029	.901	.013	3.7
		255.45	.259	.023	.902	.010	3.7
		255.95	.264	.023	.907	.010	4.4
		256.45	.262	.020	.908	.009	3.4
		256.95	.260	.021	.907	.009	3.1
		257.45	.263	.023	.899	.010	2.9
257.95	.259	.023	.897	.010	3.7		
258.45	.263	.022	.891	.010	2.6		
258.95	.261	.021	.890	.009	2.7		
259.45	.259	.023	.884	.010	2.5		
259.95	.260	.023	.882	↓	2.5		
260.45	.246	.022	.881	↓	2.3		
260.95	.251	.022	.879	↓	2.2		
261.45	.246	.021	.874	.009	2.2		
261.95	.248	.023	.874	.010	2.3		
262.45	.249	.021	.869	.009	2.5		
262.95	.238	.026	.874	.011	2.5		
263.45	.224	.026	.874	.011	2.3		

TABLE IV.— VANE SUCTION AND
 PRESSURE SURFACE CIRCUM-
 FERENTIAL LOCATIONS
 FOR HIGH TURNING CORE
 TURBINE STATOR AT
 MEAN RADIUS

Axial position, Z, percent	Suction surface location, θ_{ss} , deg	Pressure surface location, θ_{ps} , deg
0	262.28	276.13
10.0	263.42	274.77
20.0	263.51	273.96
30.0	263.25	272.90
40.0	262.66	271.75
50.0	261.59	270.40
60.0	259.97	268.85
70.0	257.85	267.37
80.0	255.29	265.50
90.0	251.96	263.47
100.0	248.22	262.07

REPORT DOCUMENTATION PAGE

Form Approved
OMB No. 0704-0188

Public reporting burden for this collection of information is estimated to average 1 hour per response, including the time for reviewing instructions, searching existing data sources, gathering and maintaining the data needed, and completing and reviewing the collection of information. Send comments regarding this burden estimate or any other aspect of this collection of information, including suggestions for reducing this burden, to Washington Headquarters Services, Directorate for Information Operations and Reports, 1215 Jefferson Davis Highway, Suite 1204, Arlington, VA 22202-4302, and to the Office of Management and Budget, Paperwork Reduction Project (0704-0188), Washington, DC 20503.

1. AGENCY USE ONLY (Leave blank)	2. REPORT DATE July 1993	3. REPORT TYPE AND DATES COVERED Technical Paper	
4. TITLE AND SUBTITLE Laser Anemometer Measurements and Computations for Transonic Flow Conditions in an Annular Cascade of High Turning Core Turbine Vanes		5. FUNDING NUMBERS WU-505-62-52	
6. AUTHOR(S) Louis J. Goldman		8. PERFORMING ORGANIZATION REPORT NUMBER E-7662	
7. PERFORMING ORGANIZATION NAME(S) AND ADDRESS(ES) National Aeronautics and Space Administration Lewis Research Center Cleveland, Ohio 44135-3191		10. SPONSORING/MONITORING AGENCY REPORT NUMBER NASA TP-3383	
9. SPONSORING/MONITORING AGENCY NAME(S) AND ADDRESS(ES) National Aeronautics and Space Administration Washington, D.C. 20546-0001		11. SUPPLEMENTARY NOTES Responsible person, Louis J. Goldman, (216) 433-5845.	
12a. DISTRIBUTION/AVAILABILITY STATEMENT Unclassified - Unlimited Subject Category 02		12b. DISTRIBUTION CODE	
13. ABSTRACT (Maximum 200 words) An advanced laser anemometer (LA) was used to measure the axial and tangential velocity components in an annular cascade of turbine stator vanes operating at transonic flow conditions. The vanes tested were based on a previous redesign of the first-stage stator in a two-stage turbine for a high-bypass-ratio engine. The vanes produced 75° of flow turning. Tests were conducted on a 0.771-scale model of the engine-sized stator. The advanced LA fringe system employed an extremely small 50-µm-diameter probe volume. Window correction optics were used to ensure that the laser beams did not uncross in passing through the curved optical access port. Experimental LA measurements of velocity and turbulence were obtained at the mean radius upstream of, within, and downstream of the stator vane row at an exit critical velocity ratio of 1.050 at the hub. Static pressures were also measured on the vane surface. The measurements are compared, where possible, with calculations from a three-dimensional inviscid flow analysis. Comparisons were also made with the results obtained previously when these same vanes were tested at the design exit critical velocity ratio of 0.896 at the hub. The data are presented in both graphical and tabulated form so that they can be readily compared against other turbomachinery computations.			
14. SUBJECT TERMS Turbomachinery; Turbine vanes; Transonic flow; Annular flow; Cascade flows; Stator vanes; Laser anemometry; Laser Doppler velocimetry		15. NUMBER OF PAGES 36	
		16. PRICE CODE A03	
17. SECURITY CLASSIFICATION OF REPORT Unclassified	18. SECURITY CLASSIFICATION OF THIS PAGE Unclassified	19. SECURITY CLASSIFICATION OF ABSTRACT Unclassified	20. LIMITATION OF ABSTRACT